Kelvin–Helmholtz Instability "Tube" and "Knot" Dynamics. Part II: KHI T&K Dynamics in a Multiscale Gravity Wave Direct Numerical Simulation

DAVID C. FRITTS[a,b] AND LING WANG[a]
[a] GATS, Boulder, Colorado
[b] Center for Space and Atmospheric Research, Embry–Riddle Aeronautical University, Daytona Beach, Florida

(Manuscript received 6 September 2022, in final form 2 May 2023, accepted 4 May 2023)

ABSTRACT: A companion paper by Fritts et al. reviews evidence for Kelvin–Helmholtz instability (KHI) "tube" and "knot" (T&K) dynamics that appear to be widespread throughout the atmosphere. Here we describe the results of an idealized direct numerical simulation of multiscale gravity wave dynamics that reveals multiple larger- and smaller-scale KHI T&K events. The results enable assessments of the environments in which these dynamics arise and their competition with concurrent gravity wave breaking in driving turbulence and energy dissipation. A larger-scale event is diagnosed in detail and reveals diverse and intense T&K dynamics driving more intense turbulence than occurs due to gravity wave breaking in the same environment. Smaller-scale events reveal that KHI T&K dynamics readily extend to weaker, smaller-scale, and increasingly viscous shear flows. Our results suggest that KHI T&K dynamics should be widespread, perhaps ubiquitous, wherever superposed gravity waves induce intensifying shear layers, because such layers are virtually always present. A second companion paper demonstrates that KHI T&K dynamics exhibit elevated turbulence generation and energy dissipation rates extending to smaller Reynolds numbers for relevant KHI scales wherever they arise. These dynamics are suggested to be significant sources of turbulence and mixing throughout the atmosphere that are currently ignored or underrepresented in turbulence parameterizations in regional and global models.

SIGNIFICANCE STATEMENT: Atmospheric observations reveal that Kelvin–Helmholtz instabilities (KHI) often exhibit complex interactions described as "tube" and "knot" (T&K) dynamics in the presence of larger-scale gravity waves (GWs). These dynamics may prove to make significant contributions to energy dissipation and mixing that are not presently accounted for in large-scale modeling and weather prediction. We explore here the occurrence of KHI T&K dynamics in an idealized model that describes their behavior and character arising at larger and smaller scales due to superposed, large-amplitude GWs. The results reveal that KHI T&K dynamics arise at larger and smaller scales, and that their turbulence intensities can be comparable to those of the GWs.

KEYWORDS: Kelvin-Helmholtz instabilities; Small scale processes; Mixing; Gravity waves; Nonlinear dynamics; Turbulence

1. Introduction

Kelvin–Helmholtz instabilities (KHI) have been studied extensively since they were first recognized in the atmosphere and oceans (Scorer 1951; Witt 1962; Woods 1968) and explored in early laboratory studies of stratified shear flows (Thorpe 1973a,b). Subsequent studies over ~45 years described idealized KHI evolutions for a wide range of Reynolds and Richardson numbers, Re and Ri, and limited Prandtl numbers, Pr. Multiple papers described the secondary instabilities of KHI in idealized narrow domains and their implications for mixing; e.g., see the reviews by Mashayek and Peltier (2012a,b) and Gregg et al. (2018). However, no previous modeling studies addressed the dynamics of adjacent misaligned or undulating KH billows.

An expanded family of secondary instabilities was revealed in laboratory shear flow experiments that enabled varying KH billow phases along their axes. These included instabilities named "tubes" and "knots" (T&K) by Thorpe (1985, 1987, hereafter T85 and T87) that led to accelerated and more intense turbulence transitions. A subsequent laboratory study by Caulfield et al. (1996) suggested that the "knots" may represent a primary instability of such shear flows. Thorpe (2002, hereafter T02) also called attention to clear evidence for KHI knots due to discontinuous and/or misaligned KH billows along their axes revealed in tropospheric clouds. Despite the accumulating laboratory, atmospheric, and oceanic evidence for KHI T&K dynamics and their potential significance, no previous modeling studies addressed these dynamics. It required another 35 years for 1) a clear KHI event exhibiting T&K dynamics to be observed in the atmosphere (Hecht et al. 2021, hereafter H21) and 2) computational capabilities enabling exploration of these T&K dynamics at sufficiently small Ri and large Re to allow their comparison with secondary convective instabilities (CI) and secondary KHI of individual KH billows (Fritts et al. 2021, 2022a,b, hereafter F21, F22a, F22b).

Denotes content that is immediately available upon publication as open access.

Supplemental information related to this paper is available at the Journals Online website: https://doi.org/10.1175/JAS-D-22-0193.s1.

Corresponding author: David C. Fritts, dave@gats-inc.com

DOI: 10.1175/JAS-D-22-0193.1

TABLE 1. List of symbols and abbreviations.

Symbols/acronym	Explanation	Symbols/acronym	Explanation
2D, 3D	Two- and three-dimensional	Pr	Prandtl number
CI	Convective instabilities	Re	Local Reynolds number
F13, F16, F21	Fritts et al. (2013, 2016, 2021)	Re_0	Bulk Reynolds number
F22a,b	Fritts et al. (2022a,b)	Ri	Local Richardson number
F23a,b	Fritts et al. (2023a,b)	Ri_0	Bulk Richardson number
FW13	Fritts and Wang (2013)	T_b	Buoyancy period
H21	Hecht et al. (2021)	x, y, z	Horizontal coordinates
KHI	Kelvin–Helmholtz instability	x', y', z'	Tilted domain coordinates
MLT	Mesosphere and lower thermosphere	u, v, w	Velocities along x, y, and z
MS(D)	Multiscale (dynamics)	ε	Kinetic energy dissipation rate
PDF	Probability density function	ω_i	Intrinsic frequency
S&L	"sheet" and "layer"	ϕ	Domain tilt w.r.t. horizontal
T85, T87, T02	Thorpe (1985, 1987, 2002)	ψ	KHI phase along x
T&K	"Tube" and "knot"	λ_2	Eigenvalue quantif. rotation
GWs	Gravity waves	λ_{KH}	KH wavelength along x
h_{KH}	KH billow half shear depth	λ_x, λ_z	Wavelengths along x and z
L	Nominal KH billow λ_x	θ, θ_0, θ'	Potential temperatures
N	Buoyancy frequency	ζ_y	Vorticity along y

Motivated by the H21 event, other imaging observations at similar altitudes (Baumgarten and Fritts 2014; Fritts et al. 2014; Hecht et al. 2014), and the initial modeling of KHI T&K dynamics, Fritts et al. (2023a, hereafter F23a) review the expanding atmospheric evidence of KHI T&K dynamics in imaging and profiling observations at ~80–90 km in the mesosphere. These results reveal that KHI T&K dynamics are virtually always present where KHI are observed at large spatial scales, and that in all cases they occur in the presence of gravity waves (GWs) that appear to contribute to the localization and alignments of the KHI responses.

Given the clear evidence for GW modulation of KHI occurrence, scales, and orientation presented by F23a, we elected to analyze a previous high-resolution DNS describing superposed multiscale (MS) GWs that further extended an earlier study by Fritts et al. (2013, hereafter F13) to a Reynolds number, Re_0, larger by 3 times, but which was not previously analyzed. The F13 results revealed clear KHI, but their character was less well defined and not explored in detail. A subsequent study by Fritts et al. (2016, hereafter F16) at an intermediate Re_0 revealed that the MS direct numerical simulation (DNS) was able to approximate "sheet" and "layer" (S&L) features observed in high-resolution soundings. F16 also revealed the occurrence of KHI and local turbulence generation by larger- and smaller-scale KHI at the highly stratified sheets between more extended, weakly stratified, layers and their significant contributions to strong turbulence and energy dissipation at earlier times.

This paper examines the occurrence of KHI T&K dynamics in a third DNS employing the same initial conditions, but for Re_0 3 times higher than assumed by F13. The model formulation, initial conditions, and computational methods are described in section 2. Section 3 describes the initial evolution to a GW/fine-structure flow comprising highly stratified sheets and weakly stratified layers (S&L features), and perturbed thereafter by the evolving GWs. The flow evolution yields smaller- and larger-scale KHI dynamics arising on various sheets described in section 4. Relations of these results to previous studies are discussed in section 5, and our conclusions are presented in section 6. A DNS application to KHI T&K dynamics addressed by F21, but not by F22a, and to increasingly viscous responses, is described by Fritts et al. (2023b, manuscript submitted to *J. Atmos. Sci.*, hereafter F23b). A list of symbols and abbreviations and their definitions is shown in Table 1.

2. Model description

a. Equations and solution methods

The DNS model we employ here is the "Triple" code previously used for lower-resolution studies of idealized GW breaking by Fritts et al. (2009) and MS GW simulations by F13, Fritts and Wang (2013, hereafter FW13), and F16. Here, we specify a bulk Reynolds number, Re_0, 3 times higher than employed by F13 to achieve higher spatial resolution of the dynamics driving turbulence at smaller scales. Nondimensionalizing with respect to an initial GW vertical wavelength λ_z, a buoyancy period T_b, and a velocity scale $U_0 = \lambda_z/T_b$, $\mathrm{Re}_0 = U_0\lambda_z/\nu = \lambda_z^2/\nu T_b = 150\,000$ and the Boussinesq Navier–Stokes equations may be written as

$$\partial\mathbf{u}/\partial t + \mathbf{u}\cdot\boldsymbol{\nabla}\mathbf{u} = -\boldsymbol{\nabla}p + \mathrm{Ri}_0\theta\mathbf{z} + \mathrm{Re}_0^{-1}\boldsymbol{\nabla}^2\mathbf{u}, \qquad (1)$$

$$\partial\boldsymbol{\theta}/\partial t + \mathbf{u}\cdot\nabla\theta = (\mathrm{Pr}\,\mathrm{Re}_0)^{-1}\boldsymbol{\nabla}^2\theta, \quad \text{and} \qquad (2)$$

$$\boldsymbol{\nabla}\cdot\mathbf{u} = 0. \qquad (3)$$

Here, $\mathbf{u} = (u, v, w)$ is the total velocity vector, p is pressure, θ is potential temperature, with a mean value θ_0, $\mathrm{Ri}_0 = N_0^2\lambda_z^2/U_0^2$ is the bulk Richardson number for mean buoyancy frequency N_0, with $N_0^2 = (g/\theta_0)d\theta_0/dz = g\beta/\theta_0$, and g the gravitational acceleration. Additionally, $\mathrm{Pr} = \nu/\kappa$ is the Prandtl number, ν is kinematic viscosity, κ is thermal diffusivity, and we assume $\mathrm{Pr} = 1$ for computational efficiency.

The kinetic and thermal energy dissipation rates are given by

$$\varepsilon = 2\mathrm{Re}^{-1}\langle S_{ij}S_{ij}\rangle \tag{4}$$

and

$$\chi = \partial_i\theta\partial_i\theta = (\mathrm{Re}\ \times\ \mathrm{Pr})^{-1}\langle\boldsymbol{\nabla}\theta\cdot\boldsymbol{\nabla}\theta\rangle. \tag{5}$$

Here, $S_{ij} = (\partial u_j/\partial x_i + \partial u_i/\partial x_j)/2$ are the symmetric components of the strain tensor, u_i are the component velocities, subscripts i and j denote the x, y, or z directions, ∂x_i denotes differentiation in the ith direction, and repeated indices imply summation.

Our solution algorithm is pseudospectral and employs high-radix fast Fourier transforms in each direction, the time integration method of Spalart et al. (1991), a variable time step (for varying velocities and resolution) with a CFL limit of 0.68, and isotropic spatial resolution constrained by $\Delta x < 1.8\eta$ (but typically $\Delta x \sim 1.6\eta$) for Kolmogorov microscale $\eta = (\nu^3/\overline{\varepsilon})^{1/4}$, throughout the DNS (Moin and Mahesh 1998; Pope 2000). For this assessment, η was evaluated every 30–50 time steps to guide required resolution changes, $\varepsilon_{\max}$ was the largest $\overline{\varepsilon}$ over any two-dimensional (2D) plane in the domain, and the spectral range was increased to achieve the new, required Δx. A "two-thirds rule" spectral truncation was also applied at each time step to avoid spectral aliasing to larger spatial scales. See F13 for further details.

b. *Simulation domain and boundary and initial conditions*

Following F13, Eqs. (1)–(3) were solved in a compact, triply periodic, three-dimensional (3D) domain inclined along the phase of an initial GW having an intrinsic frequency $\omega_i = N/10 = N\sin\phi$, with $\phi = 5.74°$, an initial nondimensional GW amplitude $a = u'_0/c = 0.5$ for phase speed $c = \omega_i/k$ (e.g., half that for incipient overturning), with initial 2D (x', z') GW wavenumber $\mathbf{k} = (k', m') = (0, -2\pi/\lambda)$ and wavelength λ along z' in the coordinate system of the inclined domain (Fig. 1).

We also assume a constant initial mean N and an initial mean fine-structure motion field in the (streamwise) plane of primary GW propagation having five cycles across the GW λ_z with $(dU/dz)_{\max} = 2N$, such that the minimum initial fine structure Ri = 1/4. The fine structure scale and amplitude were chosen to enable very small-scale KHI to arise on the stratified sheets. The specified GW and mean flow fields require a tilted domain having a length along the GW phase of $X' = Z'/(5\tan\phi) = 1.99Z'$. We define a reference length scale $L = \lambda = Z'$ and specify a spanwise domain width $Y = Y' = 0.5L$. This domain allows full definition of 3D instabilities arising due to GW breaking and KHI that arise at the resulting strongly stratified sheets. The highest model resolution required for this DNS was (5760, 1440, 2880) spectral modes.

c. *Three-dimensional visualization of vortex dynamics*

To visualize the evolving KHI T&K dynamics, we employ 3D vortex imaging revealed by the negative second eigenvalue, λ_2 (distinct from the GW wavelengths), of the tensor $\mathbf{L} = \mathbf{R}^2 + \mathbf{S}^2$, where $\mathbf{R}$ and $\mathbf{S}$ are the rotation and strain tensors, with antisymmetric components $R_{ij} = (\partial u_j/\partial x_i - \partial u_i/\partial x_j)/2$ and symmetric components defined below Eq. (5). Negative λ_2 corresponds to features having strong rotation, as opposed to shearing, and its magnitude measures rotational intensity (Jeong and Hussain 1995). In contrast, pure shearing motions do not contribute to λ_2. Negative λ_2 thus provides sensitivity to the subset of total vorticity accounting for the majority of the turbulence field. This allows us to follow the transition from initial vortex sheets to emerging vortex tubes, their interactions in knot regions driving twist waves, their fragmentation of the parent vortices, and similar interactions driving inertial-range turbulence. This method was found to provide key insights into vortex formation, interactions, twist wave forcing and evolutions, and the cascade to smaller scales in earlier GW breaking studies (Fritts et al. 1998) and in our more recent explorations of KHI T&K dynamics and energetics (F21; F22a; F22b).

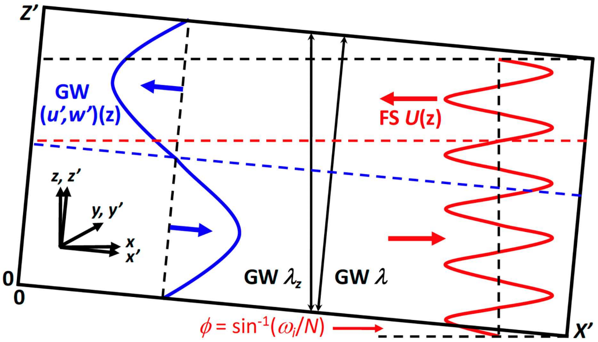

FIG. 1. The DNS computational domain aligned along the GW phase having an inclination of $\phi = \sin^{-1}(\omega_i/N) = 5.74°$ from the horizontal. The domain and geophysical coordinates are (x', y', z') and (x, y, z) shown at lower left. The initial GW u' and w' profiles are uniform along x' (blue: velocity profile; dashed: phase inclination); the initial mean $U(z)$ fine-structure field is uniform along x (red velocity profile and dashed phase inclination).

3. Modeled flow evolution and KHI T&K environments

a. *MS flow evolutions shown in 2D planes*

As in F13, the initial superposed GW and fine structure were specified to have 2D wavenumbers $\mathbf{k} = (k', m') = (0, -m_1)$ and $(k_1, -5m_1)$, respectively, where $k_1 = 2\pi/X'$ and $m_1 = 2\pi/\lambda$. These undergo a transient evolution to an MS environment exhibiting multiple GWs having larger $|m'|$, e.g., $\mathbf{k} = (0, m_1)$, $(k', m') = \pm(-k_1, nm_1)$ for $n = 1, 2, 3, \ldots$, but also larger $|k'|$ for $(k', m') = \pm(nk_1, -m_1)$ for $n = 1, 2, 3, \ldots$, in the coordinate system of the inclined domain. The responses to this transient evolution are summarized in Fig. 2 and include the following features:

1) initial 2D GW amplitudes, u' and θ', decrease 30%–40% by $\sim 7T_b$ and remain relatively constant, though oscillatory due to superpositions, to beyond $\sim 20T_b$ (Fig. 2a);
2) additional 2D GWs having wavenumbers $\pm(nk_1, -1)$, $\pm(-1, nm_1)$, and $(0, nm_1)$ for $n = 1, 2, 3, \ldots$, arise

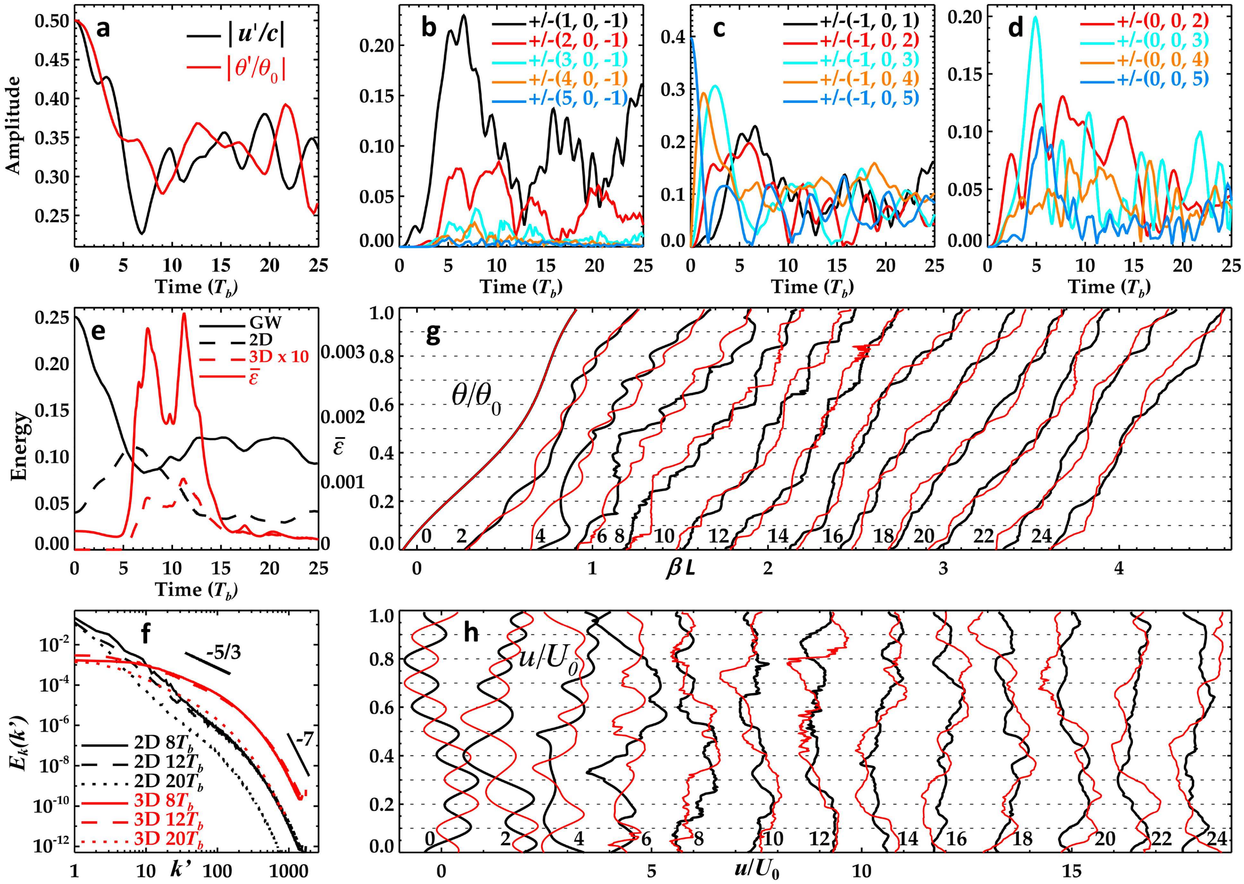

FIG. 2. Temporal variations of (a) the initial GW amplitudes with $\mathbf{k} = (k', m') = (0, -m_1)$; (b)–(d) additional modes arising at larger k' and m'; (e) primary and secondary GW total energy (black solid and dashed lines, respectively), 3D ($l' \neq 0$) total energy (dashed red line), and $\overline{\varepsilon}$ (solid red line and right-axis labels); (f) mean 2D and 3D streamwise velocity spectra (black and red, respectively) at 8, 12, and $20T_b$ (solid, dashed, and dotted, respectively); and (g),(h) vertical profiles of θ/θ_0 and u/U_0 from 0 to $24T_b$ at $x' = 0$ and $X'/2$ and $y' = 0.5Y$ (black and red lines), respectively.

by $\sim$5–$7T_b$, due to interactions among the initial modes (Figs. 2b–d);

3) 3D instabilities emerge rapidly after $\sim 5T_b$ due to strong, initial 2D interactions driving local overturning and yield accompanying large local $\overline{\varepsilon}$ (Fig. 2e);
4) 2D ($v' = 0$) and 3D domain-averaged streamwise spectra at 8, 12, and $20T_b$ are shown in Fig. 2f; 2D motions dominate the flow at horizontal scales larger than $\sim 0.1X'$ at all times whereas 3D motions are dominant at smaller scales; all motions decay significantly by $20T_b$ due to strong instabilities and large $\overline{\varepsilon}$ from $\sim$6 to $14T_b$;
5) emerging superposed 2D motions drive formation of S&L structures in θ/θ_0 and u/U_0 comprising thin, strongly stratified, and sheared vortex sheets and deep, weakly stratified and sheared layers that are most intense due to strong instabilities, turbulence, and mixing from $\sim$6 to $12T_b$ that diminish thereafter (Figs. 2g,h, respectively); and
6) strong, local turbulence is due to (i) GW breaking driving the weakly stratified layers and (ii) KHI dynamics on the vortex sheets driven by GW distortions, stretching, and intensification (Figs. 2d–f); the latter KHI dynamics are the focus of this paper.

Unlike the atmosphere, these dynamics yield decreasing instabilities and turbulence intensities with time because this initial value problem does not enable sustained GW energy inputs. The buoyancy Reynolds number reaches a peak value of $\mathrm{Re}_b = \overline{\varepsilon}/\nu N^2 \sim 50$ at times of $\sim$6, 11, and $13T_b$, the latter two at times in the evolution discussed below.

As noted above, strong transient interactions among the emerging GW modes diminish significantly by $\sim 12T_b$ and are replaced by more representative GW breaking and KHI features in an evolving MS flow exhibiting diminishing S&L structures thereafter. To explore the character and evolutions of KHI events that are more and less energetic, we investigate the KHI occurrence driven by GW dynamics during two intervals: 1) from 8 to $13T_b$ exhibiting stronger and weaker instabilities and turbulence at multiple sites and 2) from 18 to $23T_b$ having significantly weaker GW fields and S&L structures. The evolution from 8 to $13T_b$ follows the peak 2D energy, exhibits significant GW breaking and strong KHI events, and is shown with (x', z') cross sections of θ'/θ_0, N^2, spanwise (y)

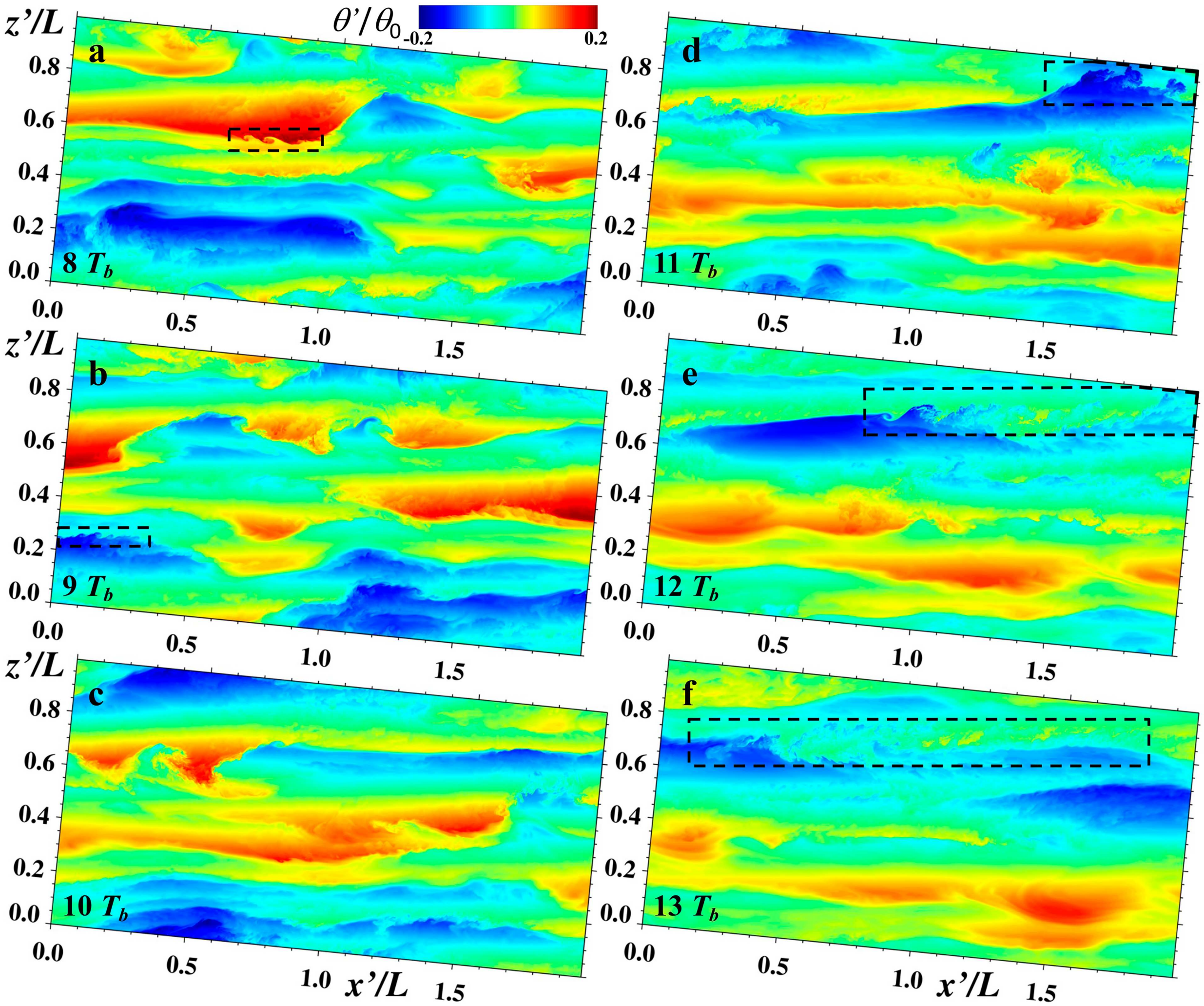

FIG. 3. $\theta'/\theta_0(x', z')$ cross sections at $y' = 0$ from (a) $8T_b$ to (f) $13T_b$. The large-scale KHI event discussed in section 4a is shown with black dashed regions. The color scale is at the top.

vorticity ζ_y, and $\log_{10}\varepsilon$ at $y = 0$ and $1T_b$ intervals in Figs. 3–6, respectively. The later, weaker evolution is shown in ζ_y at $y = 0$ from 18 to $23T_b$ at $1T_b$ intervals in Fig. 7. The image cadence in these fields is sufficient to coarsely reveal the evolution of the larger-scale GW and S&L evolutions; however, it does not resolve the evolutions of the smaller-scale KHI dynamics that evolve on time scales of a few $T_{b\max} = 2\pi/N_{\max}$, which are dictated by the N^2 at each vortex sheet at the initiation of KHI and are initially up to $\sim 10N_0^2$. We also note that KHI never arise in regions of small N^2 because these cannot acquire large $|\zeta_y|$ due to very weak GW $|du'/dz|$ where N is small.

Figures 3 and 4 reveal an MS flow exhibiting initial 1) large vertical motions and displacements at smaller horizontal scales and 2) large horizontal motions and displacements at larger horizontal and smaller vertical scales. These dynamics drive an MS S&L environment that approximates the character of high-resolution profiling revealing interleaved 1) thicker, often nearly adiabatic layers and 2) thinner, strongly sheared, and stratified sheets in the stable boundary layer, the stable troposphere, the stratosphere, and the mesosphere and lower thermosphere (MLT). Examples include in situ profiling of temperatures and winds, and radar winds and backscatter from the surface into the lower stratosphere (e.g., Balsley et al. 2018; Dalaudier et al. 1994; Doddi et al. 2022; Kantha et al. 2017; Luce et al. 1995, 2018; Muschinski and Wode 1998; Szewczyk et al. 2013; Wang et al. 2006). Contributions of the various motions evolve rapidly prior to $8T_b$ due to the unphysical initial conditions. Thereafter, the absence of GW energy fluxes into the domain from below, as would occur in the real atmosphere, result in a systematic decrease of the energy in the GW, instability, and turbulence fields. Consequences of this include weak initiation and more rapid dissipation of the emerging GWs having larger $|k'|$, more sustained energy of those having larger $|m'|$, and decreasing dissipation at later times (see the parameter evolutions in Fig. 2 discussed above).

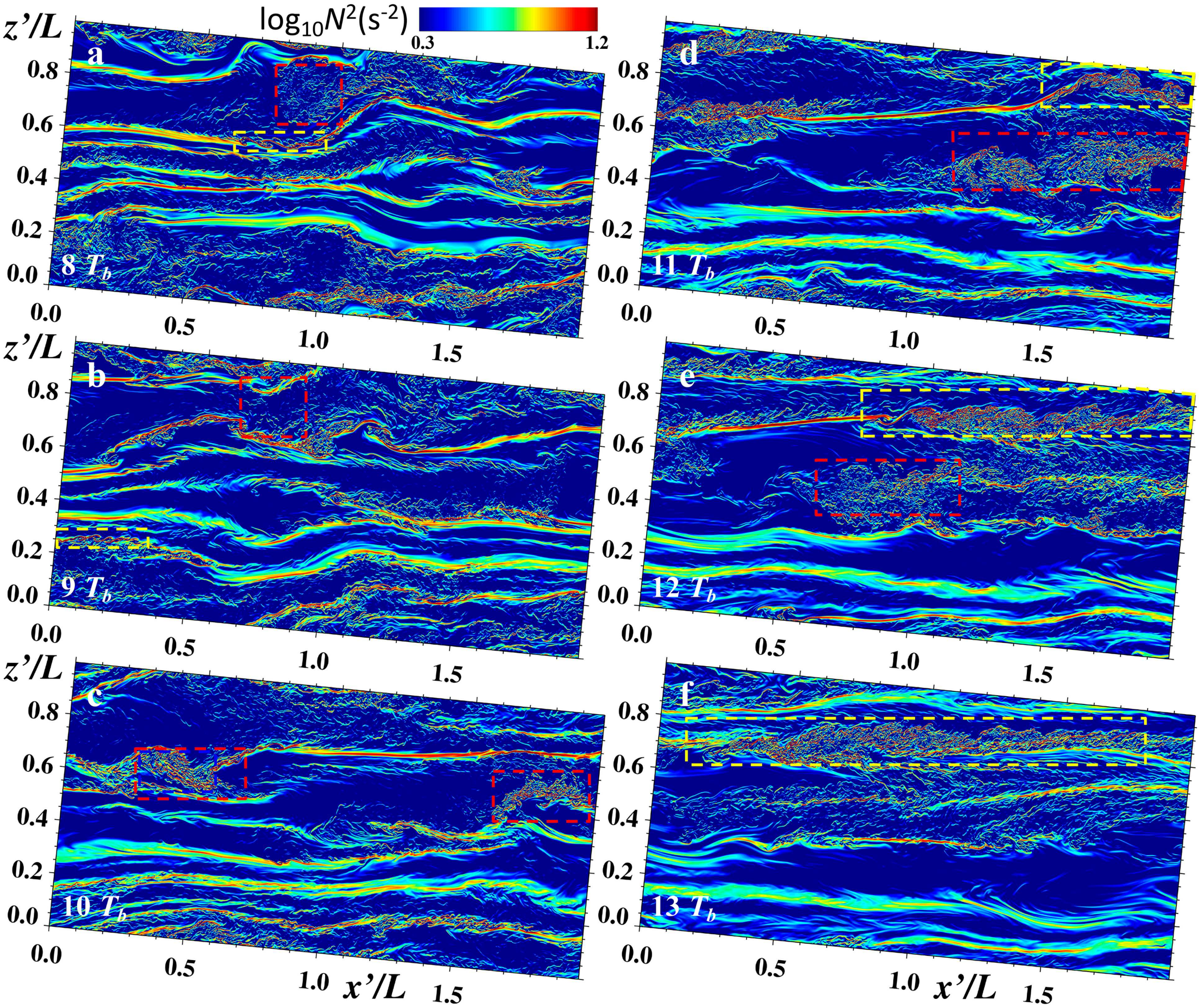

FIG. 4. As in Fig. 3, but for $\log_{10}N^2(x', z')$. Yellow (red) dashed regions highlight smaller- and larger-scale KHI (GW breaking) events discussed in the text.

Important small-scale dynamics seen in Figs. 3 and 4 from 8 to 10T_b include 1) emergence of local, small-scale KHI on highly stratified N^2 sheets at their peak vertical excursions and 2) intensification and progression of the KHI along these sheets following the peak GW displacements (see the yellow rectangles at left in Fig. 4). Also seen are larger- and smaller-scale regions extended in x exhibiting relatively uniform $T'(\theta')$ and small N^2 following peak GW vertical excursions. These result from very different GW breaking and turbulent mixing largely confined to the more weakly stratified layers (Fritts et al. 2009), but occasionally entraining the high N^2 sheets in some cases. Similar dynamics are seen to span another ~3T_b, with weaker KHI at smaller scales and stronger, larger-scale, KHI arising on, and evolving toward negative x along, the vortex sheet exhibiting the strongest stratification in the upper portion of the domain (see the yellow rectangles at right in Fig. 4). The latter event is discussed in greater detail below. These dynamics are not revealed clearly at the imaging temporal resolution in Figs. 3 and 4, but they are seen clearly in the Fig. 3 and 4 movies (P2.Fig3.mp4 and P2.Fig.4.mp4 in the online supplemental material) and others noted below.

Another perspective on these MS dynamics is provided by (x', z') cross sections of spanwise (y) vorticity ζ_y in Fig. 5. These reveal both the occurrence and orientations of the various KHI events, most of which are seen to be quite transient locally. Note that KHI events having $\zeta_y > 0$ (yellow/red) arise above and trailing the maximum upward and leftward GW velocities in the GW phase also having $\zeta_y > 0$. In contrast, KHI events having $\zeta_y < 0$ (blue) arise below and leading the maximum upward and leftward GW velocities where the GWs also have $\zeta_y < 0$. The largest induced ζ_y driving KHI in each case occurs on the highly stratified sheets rather than in the weakly stratified layers because the GW wavelength ratio varies as $\lambda_z/\lambda_x \sim \omega_i/N$ for hydrostatic GWs. The higher, trailing responses having $\zeta_y > 0$ are enhanced and sustained by GW propagation toward negative x, whereas the initial $\zeta_y < 0$

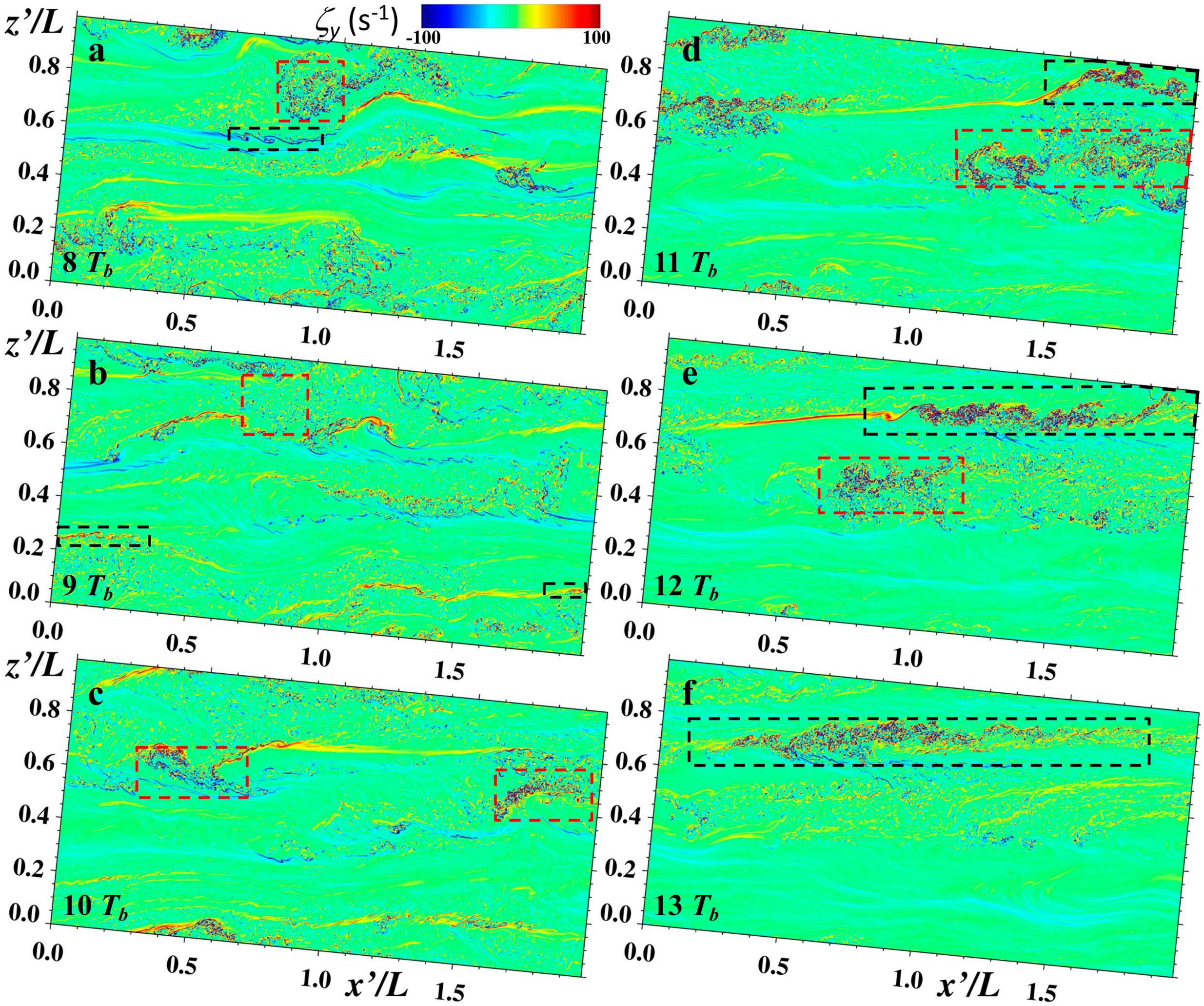

FIG. 5. As in Fig. 3, but for $\zeta_y(x', z')$. Black (red) dashed regions highlight smaller- and larger-scale KHI (GW breaking) events discussed in the text.

responses are often overtaken and reversed by the advancing GWs; see the yellow (black) rectangles at left in Fig. 4 (Fig. 5). In each case, the GW motions stretch and intensify the KHI on the vortex sheet at its upper and lower extrema.

These dynamics are precursors of GW breaking events that often entrain adjacent KHI and exhibit various forms, depending on the GW scales and superpositions. The major responses from ~8 to $11T_b$ exhibit KHI formation and GW breaking followed by plunging and rapid expansion of the turbulent regions exhibiting strong, very-small-scale ζ_y of both signs (see the regions above and below the strong vortex sheets in Fig. 5 highlighted with red rectangles). The events evolve to weaker, larger-scale forms extending another ~$10T_b$ thereafter.

Seen emerging by $11T_b$ are large-scale KH billows on the strongly stratified vortex sheet in the upper-right portion of the displayed domain (see the black and yellow rectangles at right in Figs. 3–5). These arise in the same manner as the previous smaller-scale events accompanying an elevated GW phase, but in this case for a larger-scale GW impacting a more highly stratified sheet enabling stronger GW-induced shears. These dynamics yield an evolving KH billow train spanning ~$2T_b$ (see the Figs. 5 and 7 movie P2.Fig5&7.mp4 from 8 to $23T_b$).

The significance of this KHI event is illustrated in Fig. 6, which shows $\log_{10}\varepsilon(x', z')$ cross sections at $y = 0$ enabling comparisons of the turbulence intensities arising due to GW breaking and KHI from 8 to $13T_b$; red and black regions highlighting $\log_{10}\varepsilon$ due to two GW breaking events and the large-scale KHI event are labeled 1, 2, and 3, respectively. Large $\log_{10}\varepsilon(x', y', z')$ due to all three events are localized and transient. Probability density functions (PDFs) of $\log_{10}\varepsilon$ for these regions shown at bottom in Fig. 6 exhibit strong contributions from these events, and weaker, also roughly lognormal, PDFs from previous turbulence events, with black, blue, and red from earlier to later times, respectively. To estimate

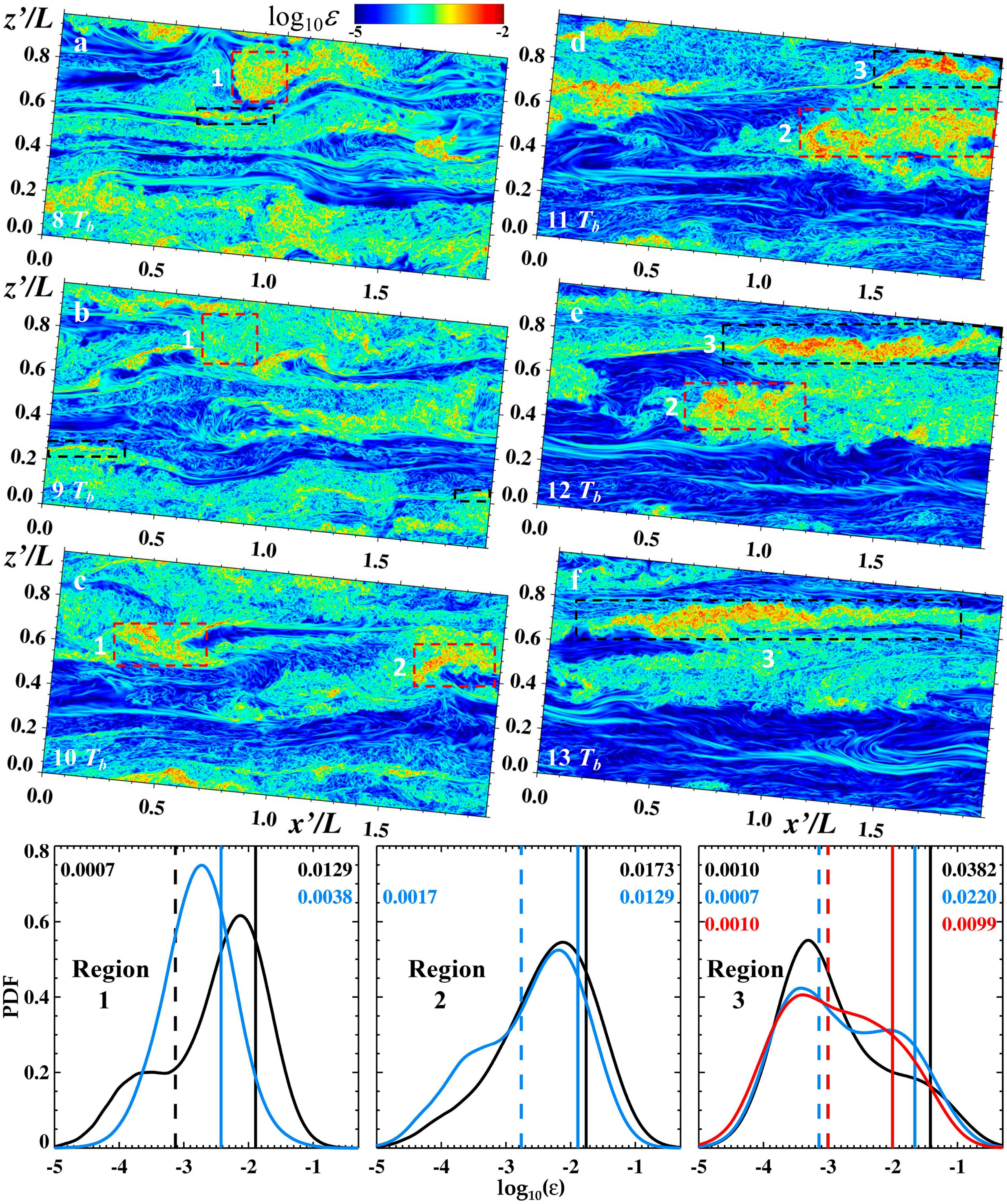

FIG. 6. (a)–(f) As in Fig. 3, but for $\log_{10}\varepsilon(x', z')$. Black (red) dashed regions highlight the larger-scale KHI (GW breaking) events discussed in the text. (bottom) The $\log_{10}\varepsilon$ PDFs computed in the GW breaking regions labeled 1 and 2 at two times and in the region of large-scale KHI labeled 3 at three times, all spanning the full y domain. See text for details.

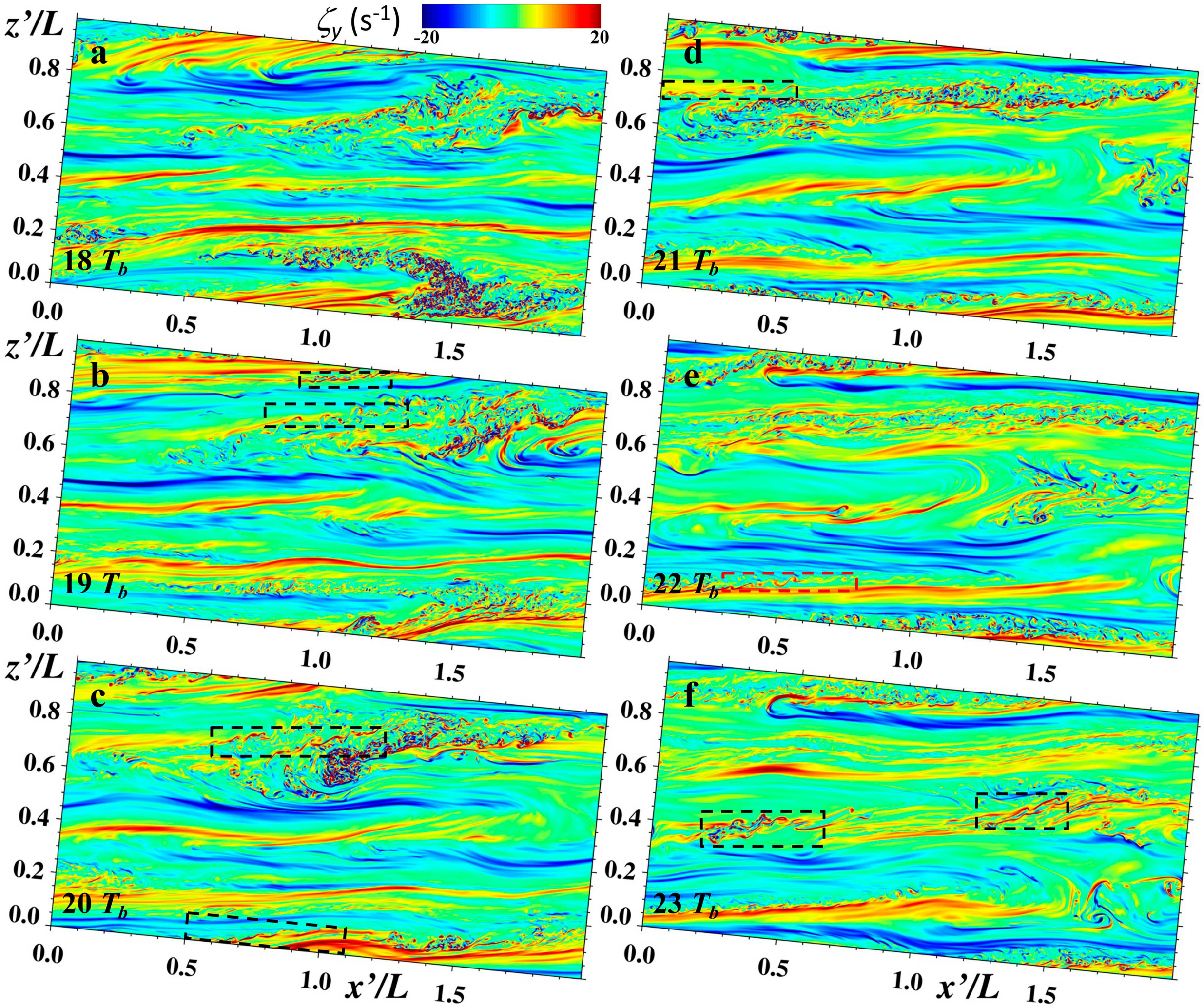

FIG. 7. As in Fig. 5, but for $\zeta_y(x', z')$ from (a) 18T_b to (b) 23T_b. Black dashed regions highlight several smaller-scale KHI events discussed in the text. The red dashed region at 22T_b highlights the later event also seen to exhibit T&K dynamics in Fig. 12. Note that the smaller color scale is different than that in Fig. 5.

and compare $\overline{\varepsilon}$ due to the concurrent GW breaking and large-scale KHI events, we assume separate lognormal distributions for these events, and for the background turbulence in each case, and perform joint fits to the PDFs in each region where they reveal two maxima.

Inferred $\overline{\varepsilon}$ for the three events at each time are shown with vertical lines and values listed at upper right in each panel. Inferred weaker, background $\overline{\varepsilon}$ are shown with dashed lines and values listed at upper left where a second PDF peak occurs. This assessment reveals the KHI event to achieve maximum $\overline{\varepsilon}$ that are ~2–5 times larger than for the earlier and coincident GW breaking events. Similar events occurring at much smaller scales also extend to much later times. These results imply potentially significant roles for KHI dynamics in mixing relative to GW breaking in MS dynamics that are not widely appreciated, nor directly parameterized at present, in current models. P2.Fig6.mp4 shows an animation of Fig. 6 at top from 8 to 23T_b.

MS dynamics weaken as the finite initial energy is dissipated by GW breaking and KHI events. This causes the dominant motions to become more nearly horizontal and manifest as the "intrusions" described initially by F13 at a smaller Re at later times. These motions continue to excite weak, smaller-scale KHI at their edges that dissipate the remaining kinetic and potential energy at a slower rate. A later, weaker stage of this DNS is shown in ζ_y at $y = 0$ from 18 to 23T_b at 1T_b intervals (see the highlighted regions in Fig. 7 and movie P2.Fig5&7.mp4). The smaller-scale KHI event highlighted in red at 22T_b is also examined further below in order to assess to what degree KHI T&K dynamics extend to smaller scales and Re.

b. S&L evolutions and implications for KHI scales and intensities

MS GW dynamics described above were seen to drive the formation of S&L structures that enable KHI to arise on

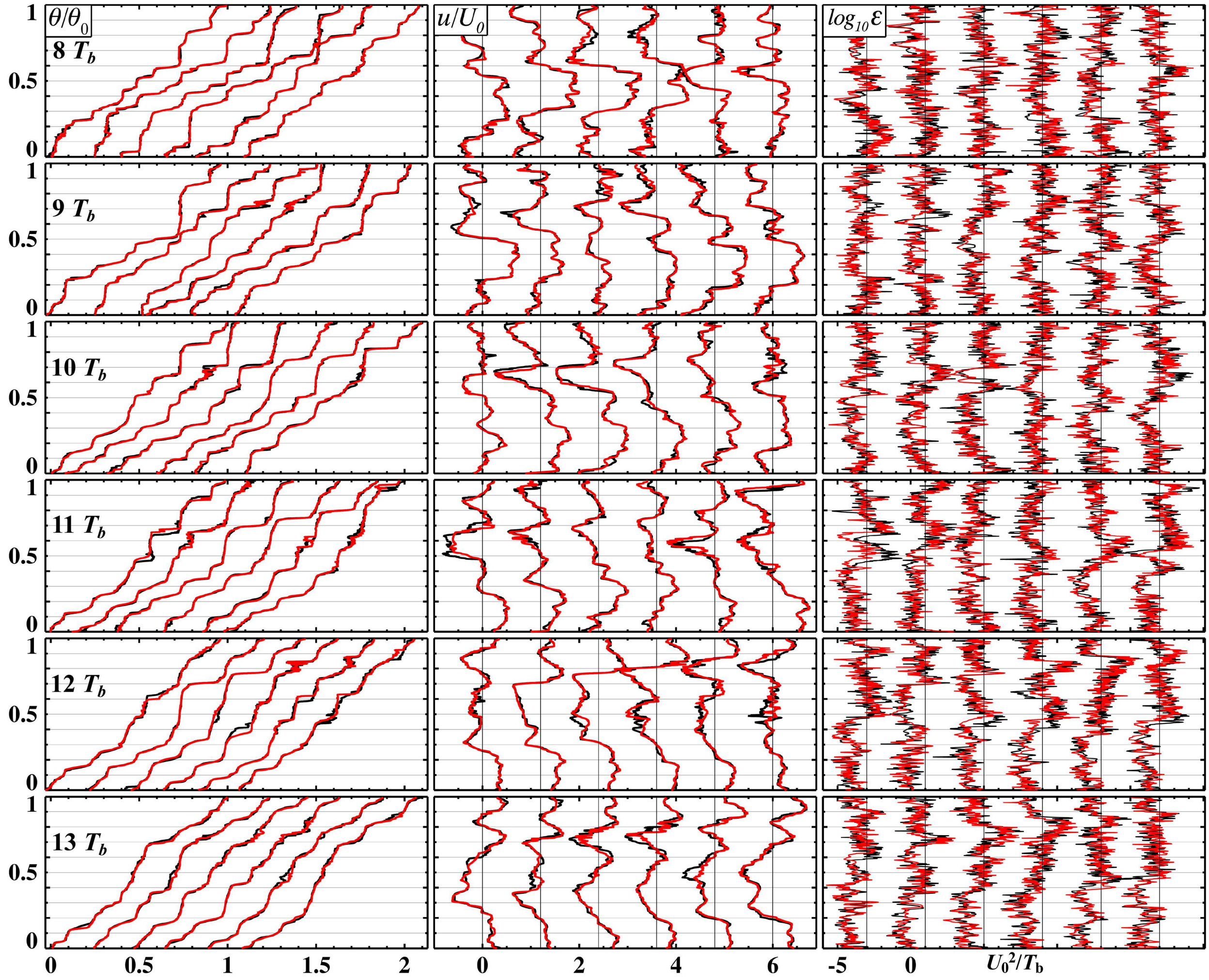

FIG. 8. As in Figs. 2g and 2h, but showing profiles of (left to right) θ/θ_0, u/U_0, and $\log_{10}\varepsilon$ from (top to bottom) $8T_b$ to $13T_b$ at six locations along x' and at $y' = 0$ and $Y/2$ (red and black, respectively). Vertical lines in the center and right columns show $u/U_0 = 0$ and $\log_{10}\varepsilon = -3U_0^2/T_b$ at each site.

multiple scales and have both positive and negative ζ_y. Additional insights into their environmental dependence and implications for ε are provided by vertical profiles of θ/θ_0, u/U_0, and $\log_{10}\varepsilon$ from 8 to $13T_b$ at six x' locations in the (x', z') planes at $y' = 0$ and $Y/2$ in Fig. 8. The θ/θ_0 profiles exhibit S&L structures at all locations and times comprising thin, strongly stratified sheets separated by thicker, weakly stratified layers. Those at 8–$10T_b$ exhibit multiple thinner and thicker nearly adiabatic layers indicating a complex MSD environment with multiple, superposed GW modes yielding multiple regions experiencing incipient, active, or recent turbulence and mixing. The profiles at 11 and $12T_b$ have larger layer depths due to the very active KHI and GW breaking regions discussed above. Those at $13T_b$ exhibit smaller, less pronounced sheets and more stable layers, apart from the large KHI event.

Corresponding u/U_0 profiles show the highly stratified sheets to coincide with large $|du/dz|$ because GWs cannot induce strong shears in weak stratification, as noted above. Also seen are multiple cases in which 1) the sheets exhibit fine structure due to local KHI overturning or induced turbulence and 2) the layers exhibit deep turbulence due to active or previous GW breaking yielding primarily small turbulence scales. Earlier, energetic GW breaking becomes less pronounced during this interval because of the “spindown” character of the initial value MS GW field. This results in fewer, weaker S&L features and decreasing $|du/dz|$ at later times, apart from the still active large-scale KHI event emerging in region 3 of Fig. 6 at $11T_b$.

The ε profiles at right reveal significant large- and small-scale variability, with ε varying over up to five decades at closely spaced depths where the instability events are strongly layered. The stronger, earlier GW breaking events exhibit peak $\varepsilon \sim 0.1U_0^2/T_b$, and somewhat larger in small regions. The large-scale KHI event described above and examined in greater detail below achieves comparable, and in some regions even larger ε, suggesting, in this DNS at least, that KHI can be competitive with larger-scale GW breaking in driving turbulence and mixing.

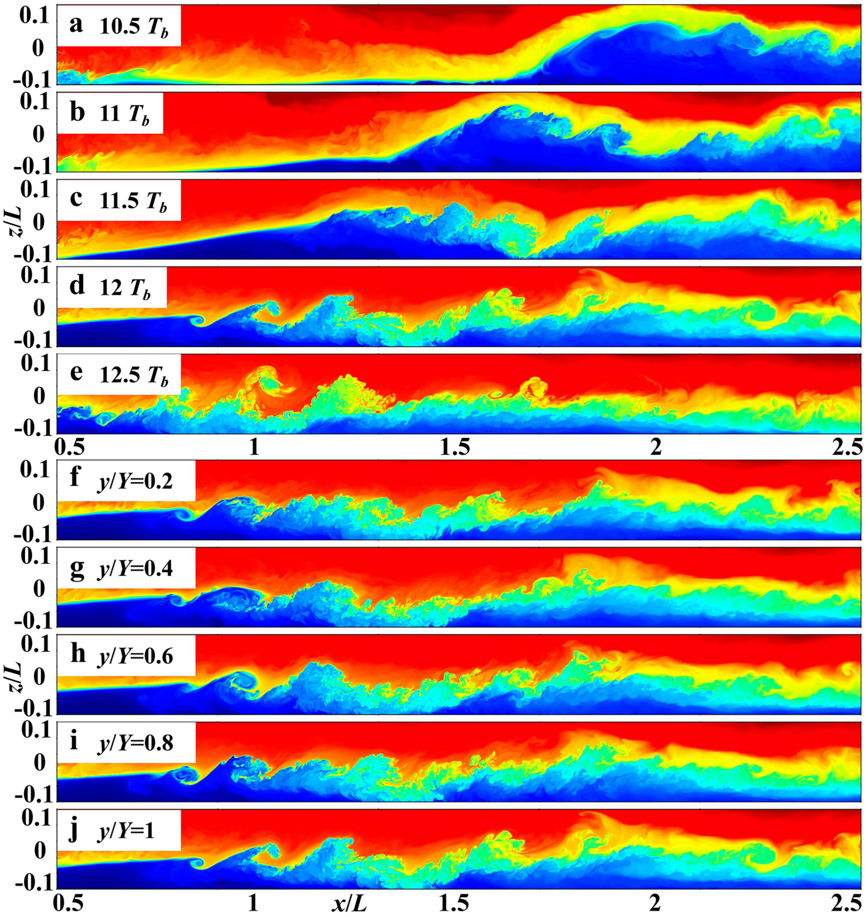

FIG. 9. (a)–(e) $\theta/\theta_0(x, z)$ from $10.5T_b$ to $12.5T_b$ at $y = 0$ (1) for the KHI event in the black dashed regions in Fig. 6. (f)–(j) These dynamics for $y/Y = 0.2$, 0.4, 0.6, 0.8, and 1 (0) at $12T_b$. The color scale is as in Fig. 3.

4. KHI T&K dynamics arising in an idealized MS DNS

Our discussion above identified a diversity of KHI events arising in an initial 2D motion field determined by transient, 2D responses to initial wave–wave and wave–mean flow interactions. The subsequent flow was influenced by 3D instabilities, turbulence, and mixing due to GW breaking and the induced KHI. The KHI responses include

1) the large-scale KHI event seen in Figs. 3–6 arising in response to a large-horizontal-scale GW perturbation of a relatively uniform sheet having very strong N^2, and
2) multiple smaller-scale KHI responses to GW vortex sheet deformations having varying N^2 and horizontal extents that decrease in their wavelengths and intensities with time, and which account for weaker, but significant, energy dissipation at later times.

a. Large-scale KHI T&K dynamics

We first examine the large-scale KHI event because it induces local ε comparable to, or larger than, the GW breaking events at these times. The large scales imply a large KHI Reynolds number, $\mathrm{Re}_{\mathrm{KH}} = U_{\mathrm{KH}}h_{\mathrm{KH}}/\nu$, for U_{KH} the half-shear velocity difference, h_{KH} the half-shear depth, and ν the kinematic or turbulence viscosity. Specifically, we expect the KH billow wavelength to increase from $\lambda_{\mathrm{KH}} \sim 2^{3/2}\pi h_{\mathrm{KH}}$ as the initial Ri decreases from 0.25 (Drazin 1958) and the KH billow depth D to increase from ~0.2 to 0.5 λ_{KH} as Ri decreases from ~0.15 to 0.07 (Thorpe 1973a) for Re > 1000. Also assuming a nominal Ri = 0.07 consistent with an observed $D/\lambda_{\mathrm{KH}} \sim 0.5$ at peak D, $N^2 \sim 10N_0^2$ at the strong vortex sheet, varying KHI $\lambda_{\mathrm{KH}} \sim 0.1$–$0.25L$, and an inferred $U_{\mathrm{KH}} \sim 12N_0h_{\mathrm{KH}}$, we obtain an estimated $\mathrm{Re}_{\mathrm{KH}} \sim 1000$–$6000$. This range ensures the occurrence of secondary convective instability dynamics anticipated from previous laboratory, theoretical, and modeling studies discussed above. The larger $\mathrm{Re}_{\mathrm{KH}}$ should also enable secondary KHI on the vortex sheets between, and wrapping around, the larger-scale KH billow λ_{KH}, especially where they arise having initial Ri ~ 0.07 or smaller, $\lambda_{\mathrm{KH}} \sim 0.2L$ or larger, or are intensified by stretching in close proximity to KHI knots (see F23b). At the smaller λ_{KH},

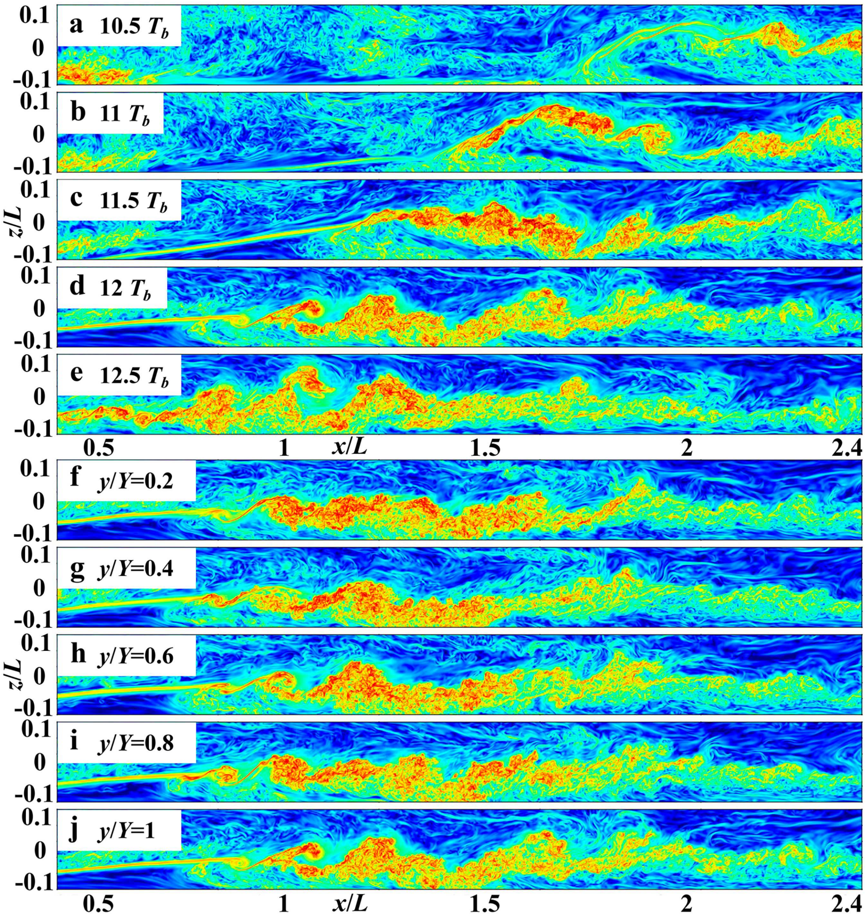

FIG. 10. As in Fig. 9, but showing (a)–(e) $\log_{10}\varepsilon(x', z')$ from $10.5T_b$ to $12.5T_b$ at $y = 0$ (1) for the KHI event in the black dashed regions in Fig. 6. (f)–(j) These dynamics for $y/Y = 0.2$, 0.4, 0.6, 0.8, and 1 (0) at $12T_b$. The color scale is as in Fig. 6.

however, we expect that secondary KHI will be suppressed and these billows will exhibit weaker interactions and smaller ε.

The KHI evolution is shown in $\theta/\theta_0(x, z)$ and $\log_{10}\varepsilon\ (x, z)$ cross sections spanning the shear layer from 10.5 to $12.5T_b$, at $y/Y = 0$, and at $y/Y = 0.2$, 0.4, 0.6, 0.8, and 1 at $12T_b$, in the upper and lower panel sets of Figs. 9 and 10, respectively. The upper panels of Fig. 9 reveal various features of this KHI event relevant to our interests here. These include the following:

1) KHI peak responses occur following rising GW phases (upward and toward smaller x) at the peak upward GW displacements that yield the strongest horizontal divergence, the most intense shears, and positive (yellow/red) ζ_y in Fig. 5,
2) adjacent KH billow $\lambda_{\rm KH}$, D, $D/\lambda_{\rm KH}$, and secondary KHI exhibit significant variability along the vortex sheet at each time suggesting highly variable initial $h_{\rm KH}$ and Ri,
3) peak KH billow $D/\lambda_{\rm KH} \sim 0.8$ reveal occasional, very small initial Ri and strong T&K influences, including vortex tubes between adjacent billows and frequent, large-scale secondary KHI (see the cross sections at 12 and $12.5T_b$ from $x/L \sim 0.7$ to 1.7), and
4) KHI secondary instabilities decrease in intensity, but KHI T&K dynamics persist as billow scales and Re decrease.

The lower panels of Fig. 9 reveal major variations in the KHI features along x at $\Delta y = 0.2L$ (comparable to the local $\lambda_{\rm KH}$) in billow locations, stages of their evolutions, and the character of secondary instabilities that imply strong T&K dynamics at essentially all locations.

The corresponding evolution of this KHI event in $\log_{10}\varepsilon\ (x, z)$ cross sections is shown in Fig. 10. Additional insights include the following:

1) the largest ε arise in the KH billows having the largest D and $\lambda_{\rm KH}$ and smallest Ri;
2) larger ε are seen in KH billow or former larger-scale vortex tube cores that are already relatively well mixed and have only weak gradients in the $\theta'/\theta_0(x, z)$ fields;
3) peak KHI ε at ~10.5–$12.5T_b$ are larger than the peak values arising due to GW breaking at these times; see Fig. 6 and the regions above the shear layer in Fig. 9; and
4) ε fields reveal large T&K variations along y more clearly than seen in $\theta'/\theta_0(x, z)$ fields.

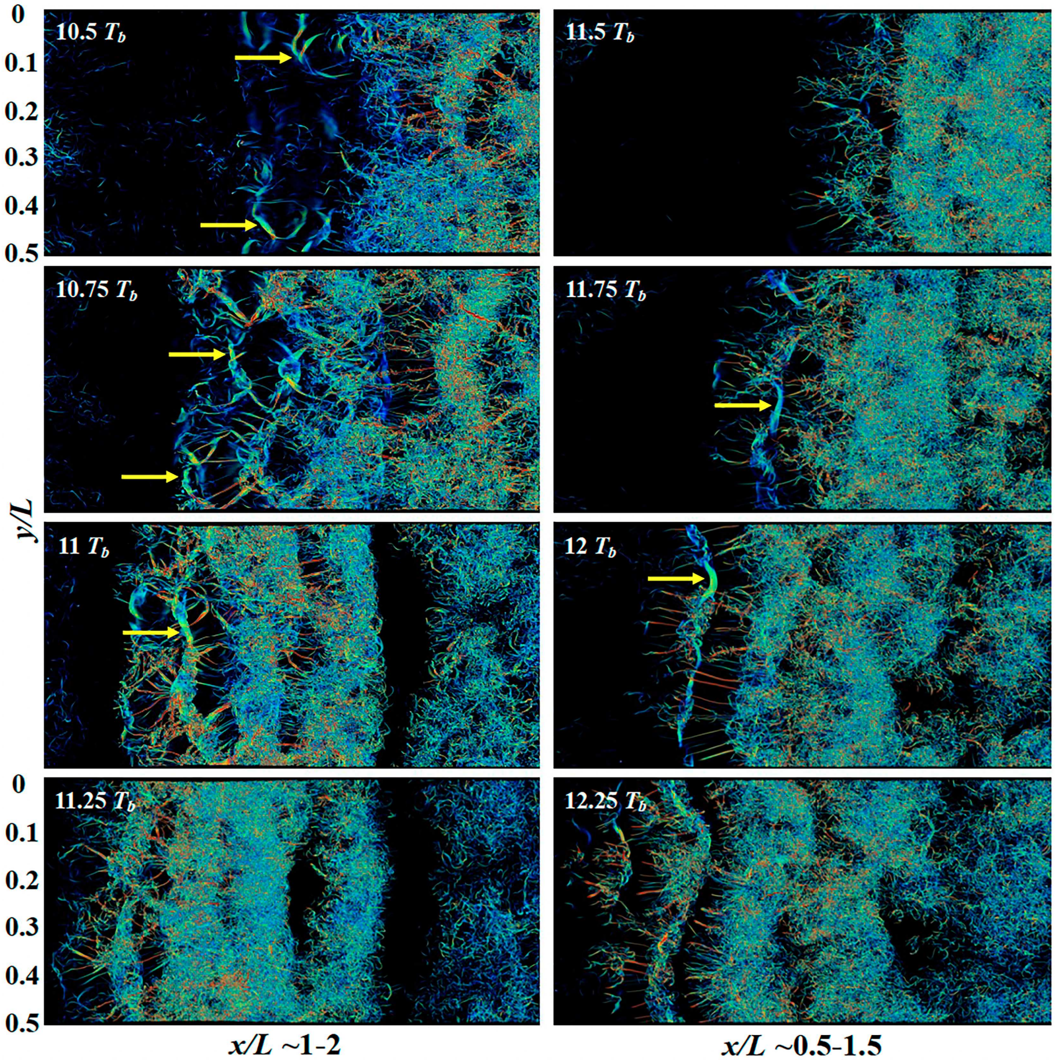

FIG. 11. Three-dimensional imaging of the larger-scale KHI event employing λ_2 shown in the yellow (black) regions at right in Figs. 4 (Figs. 5 and 6). The λ_2 fields are shown viewed from below with each spanning $0.75T_b$ at intermediate and later times in this event. λ_2 has no dimensions, but increasing negative values (e.g., green, yellow, and red) show increasing rotation. Yellow arrows indicate initial KH billow cores prior to strong T&K dynamics driving their breakdown.

To explore the KHI T&K dynamics accounting for the 2D fields described above more quantitatively, we now employ volumetric 3D imaging of these dynamics revealed by $\lambda_2(x, y)$ viewed from below. Those accompanying the large-scale KHI event highlighted in Figs. 3–6 are shown for two regions ($x/L \sim 1$–2 and ~0.5–1.5) viewed from below at 10.5–11.25 and 11.5–$12.25T_b$ in the left and right columns, respectively, in Fig. 11. Zoomed views of the leading edges of these responses at higher temporal resolution highlight the evolutions of key features in two intervals in Fig. 12. A further zoomed view of the leading edge of the later response in Fig. 12 is shown at $12.25T_b$ in Fig. 13. For these cases, 3D imaging of $\lambda_2(x, y)$ is confined to the thin layer containing the evolving KHI having a depth $\Delta z = 0.2L$ in order to exclude responses due to other dynamics above and below.

The leading edge of the KHI progression toward smaller x is shown in Fig. 11 with successive images shifted to compensate for large-scale motion of the shear layer. Yellow arrows highlight portions of emerging KH billow cores that arise from the initial perturbations that are highly variable along y and account for the emerging T&K features thereafter. This evolution exhibits multiple subsequent, undulating KH billow cores revealing a progression to smaller KHI λ_x at smaller x that span the model domain thereafter and contribute multiple examples of T&K dynamics driving the transitions to turbulence. Note, in particular, the multiple occurrences of "X"- and "Y"-shaped features at larger scales that exhibit strong turbulence transitions within the following $0.25T_b$. These very rapid transitions to strong turbulence are due to the much shorter time scales dictated by the significantly

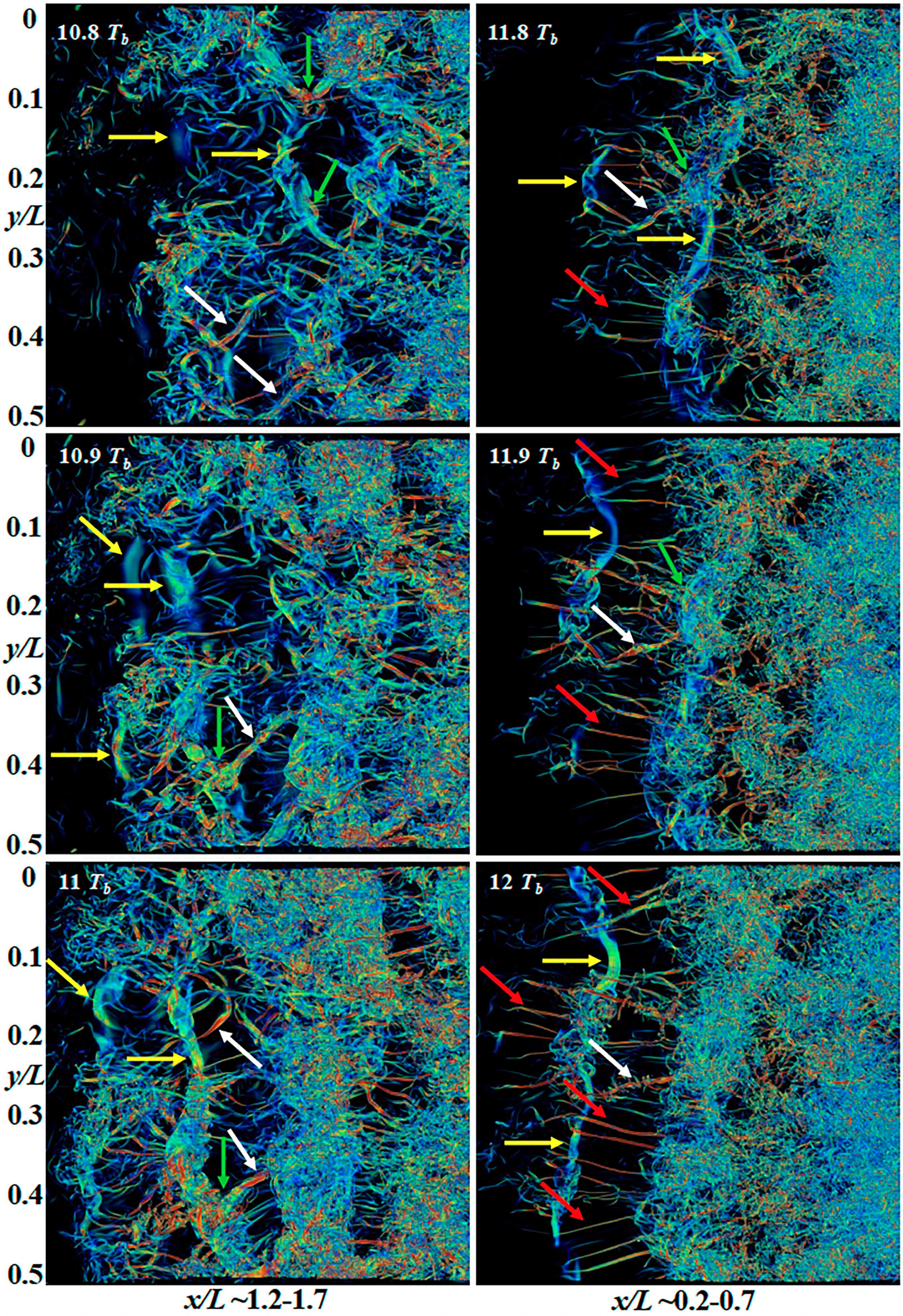

FIG. 12. Zoomed views of the leading edges of the regions shown in Fig. 11 at higher temporal resolution (left) from $10.8T_b$ to $11T_b$ and (right) from $11.8T_b$ to $12T_b$. Yellow arrows are as in Fig. 11. White, red, and green arrows show examples of larger- and smaller-scale vortex tubes linking adjacent KH billow cores and emerging vortex knots arising due to intense vortex interactions.

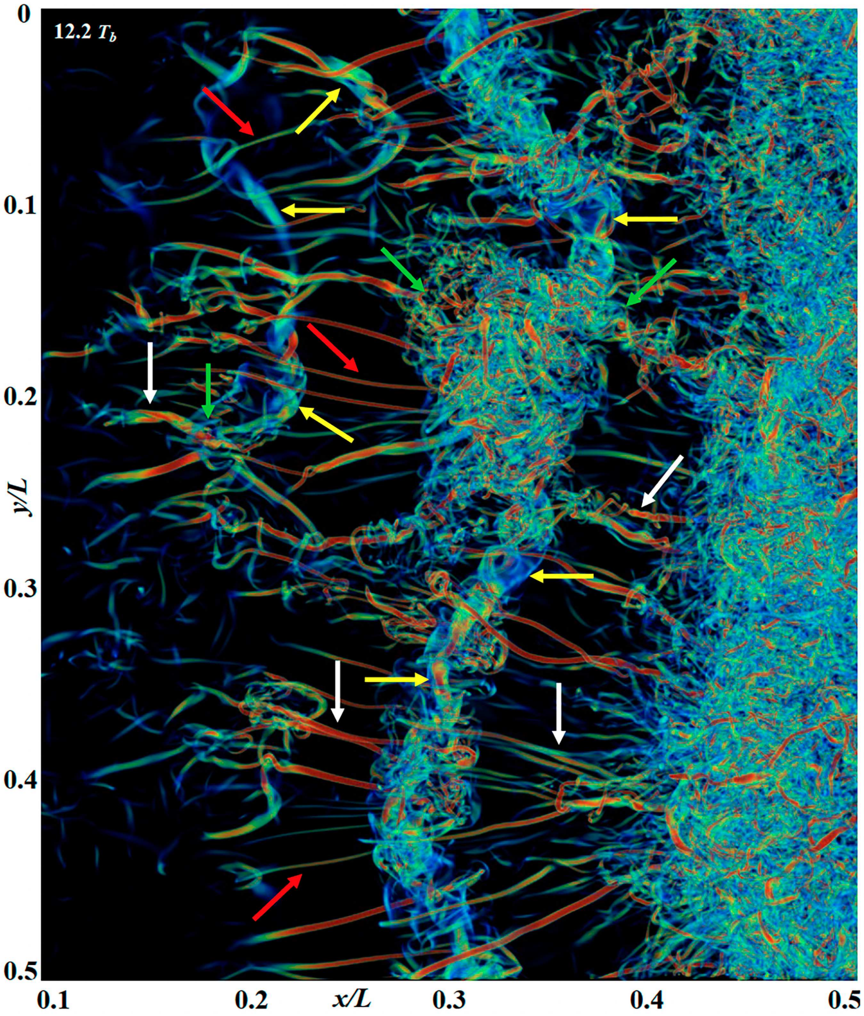

FIG. 13. As in Fig. 12, but showing a further zoomed view at $12.2T_b$ to more clearly reveal the various components of the vorticity field accompanying KH billow breakdown via T&K dynamics. Arrow codes are as in Figs. 11 and 12.

stronger stratification of the vortex sheet driving the KHI evolution. An animation of this event is shown in P2.Fig11-13.mp4.

Figure 12 shows two sets of $\lambda_2(x, y)$ images, each spanning only $0.2T_b$, that show representative T&K dynamics at higher temporal resolution with greater detail. Earlier and later sequences at left and right show KHI T&K dynamics for stronger and weaker GW modulations of the initial strongly stratified sheet and emerging shear layer. The earlier of these exhibits local, weak emerging billows; the later series shows these dynamics clearly.

The image at $10.8T_b$, top left in Fig. 12, exhibits significant evidence of earlier misaligned KH billow cores due to their phases ψ along x that vary along y (as distinct from the initial GW phase inclination, ϕ) that lead to 1) very short billow coherence along y, 2) apparent ringlike features where KH billows link via vortex tubes, forming knots, at short distances along y, and 3) rapid transitions to intense, small-scale turbulence thereafter. Several examples of emerging billow cores, large-scale vortex tubes where KH billows are significantly misaligned, and vortex knots arising where billow cores and large-scale vortex tubes link are shown with yellow, white, and green arrows, respectively, in Figs. 11–13.

The image sequence in the right column in Fig. 12 reveals these dynamics at a later stage, and in a less disturbed shear layer environment (see the fields at $12T_b$ in Figs. 4–6). Seen at right are emerging KH billow cores exhibiting varying phases ψ but no significant misalignments, along y (yellow arrows). Thin, initial vortex tubes emerge on the vortex sheets between adjacent billow cores having roughly orthogonal alignments to the billow cores exhibiting more weakly varying phases (red arrows). Larger-scale vortex tubes arise on the vortex sheets where billow cores exhibit larger $|d\psi/dy|$ and are also roughly orthogonal to the billow cores in these regions (white arrows). As these various dynamics intensify, they undergo strong interactions with neighboring vortices, and these are especially intense where billow cores and large-scale

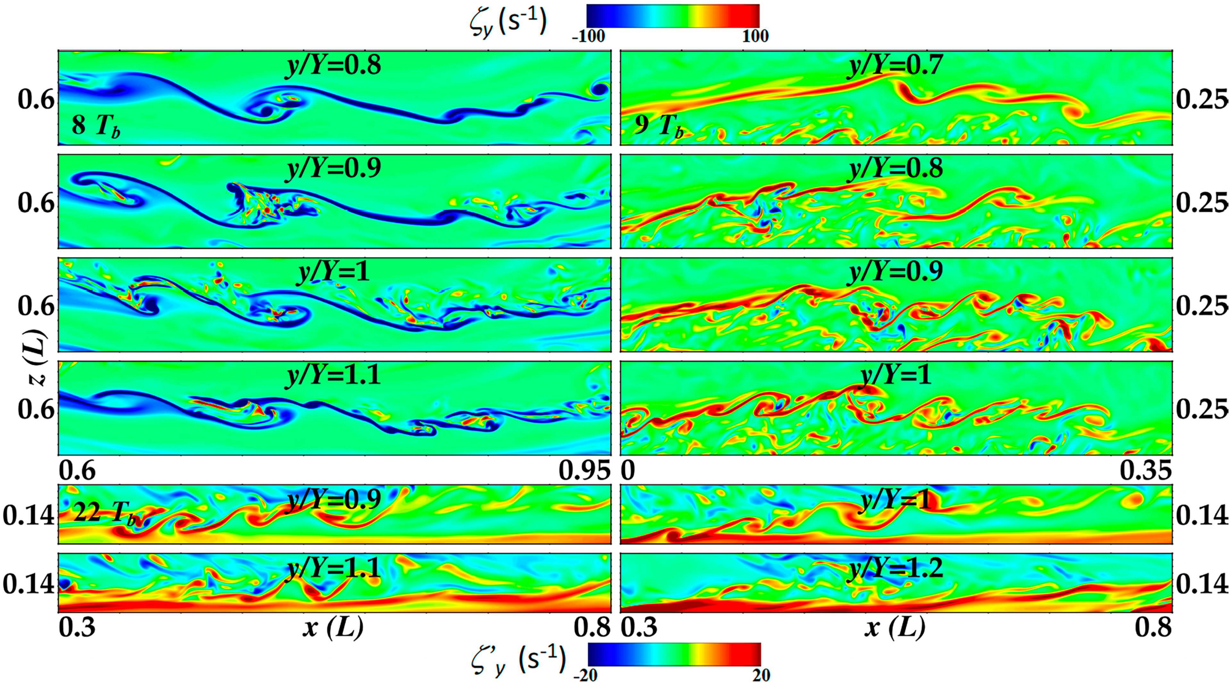

FIG. 14. Expanded views of $\zeta_y(x, z)$ (left) in the black rectangles at $8T_b$ and $9T_b$ in the left column of Fig. 5 and (right) in the red rectangle at $22T_b$ in right column of Fig. 7. Each sequence spans a width of $0.3Y$ that exhibits significant variability along y revealing additional KHI T&K dynamics extending to very small scales and Re.

vortex tubes link to form rapidly evolving and intensifying vortex knots (green arrows) that expand to span the entire KH billow core at later times (see the images at $10.9T_b$ and $11T_b$).

A zoomed, further evolved field (at $12.2T_b$) at the leading (left) edge of the emerging KHI T&K dynamics at smaller x is shown in Fig. 13. This reveals these various dynamics more clearly using the same labels. As above, emerging laminar billow cores and large-scale vortex tubes are shown with yellow and white arrows, respectively. These features exhibit perturbations in multiple regions that reveal initial twist waves at larger and smaller scales, which act to break up these initially coherent structures thereafter. Vortex knots arise where these vortex interactions progress quickly (green arrows) and drive a rapid cascade to smaller scales in the turbulence inertial range. Where the flow remains laminar, thin vortex tubes continue to arise on the distorted vortex sheets wrapping over and under adjacent KH billows (red arrows). Also see the more detailed descriptions of these dynamics in a more idealized, higher-resolution DNS by F23b.

b. *Small-scale KHI T&K dynamics*

Finally, we explore whether KHI T&K dynamics also arise on thinner and weaker vortex sheets within the larger-scale MSD. The events examined are those highlighted with yellow and black rectangles at left in Figs. 4–6 at $8T_b$ and $9T_b$, and with a red rectangle at $22T_b$ in Fig. 7. As at bottom in Figs. 9 and 10, $\zeta_y(x, z)$ cross sections spanning a $0.3Y$ portion of the spanwise domain including $y/Y = 1$ are shown for each region in Fig. 14. Inspection of these cross sections reveals that strongly varying KH billow scales and locations along y also extend to much smaller scales and Re, as seen for the larger-scale KHI T&K event discussed above. These fields demonstrate that T&K dynamics appear to accompany KHI wherever they arise on strongly stable vortex sheets intensified by the larger-scale MS GW environment. Their extension to smaller Re will be examined in greater detail by F23b.

5. Discussion and relation to previous studies

F23a presented extensive evidence for widespread KHI T&K dynamics in OH airglow and polar mesospheric cloud imaging and lidar profiling at ~80–90 km in the MLT. Additional evidence was noted in lidar, radar, and in situ profiling in the stable boundary layer, troposphere, and stratosphere, and in acoustic and in situ profiling in the oceans, spanning many years. That survey was motivated by multiple factors suggesting potentially significant, but largely unappreciated, influences of these dynamics on the local and large-scale structure and variability of the atmosphere from the surface into the thermosphere. Key insights from F23a include the following:

1) laboratory demonstrations of the occurrence and rapid evolutions to turbulence by KHI T&K events relative to secondary CI and KHI of individual KH billows (T85, T87),
2) the T02 evidence that these dynamics should be widespread in the atmosphere,
3) recent observations of dramatic KHI events reported by H21 and Kjellstrand et al. (2022) revealing various T&K dynamics and their evolutions at smaller spatial scales,

4) evidence that GWs play key roles in defining KHI T&K environments, and
5) new, and revisited, imaging and profiling revealing KHI T&K events to be widespread and often exhibiting KH billow $\lambda_{\mathrm{KH}} \sim 5$–15 km in the MLT.

Specific examples of item 5 include previous polar mesospheric cloud and OH imaging described by Baumgarten and Fritts (2014), Fritts et al. (2014), and Hecht et al. (2014) that revealed key elements of these dynamics, evolutions suggesting T&K dynamics, and clear GW influences, a number of which were recognized only in hindsight.

Despite much earlier laboratory studies and atmospheric observations revealing the importance of KHI T&K dynamics (T85; T87; T02), and the extensive evidence for such reviewed by F23a, the first modeling study designed to address these dynamics was the idealized large-eddy simulation (LES) by F21. Earlier LES of mixing-layer dynamics in large domains by Comte et al. (1998) and Balaras et al. (2001) exhibited clear KHI T&K dynamics, specifically misaligned billows along their axes and vortex tubes linking adjacent billows. But these studies neither recognized these T&K dynamics, nor related them to the earlier laboratory results. A more recent, large-domain DNS by Watanabe and Nagata (2021) addressing late-time vortex structures arising in shear flows serendipitously revealed clear T&K dynamics at earlier times, but these dynamics were not the focus of that study. The authors noted that these dynamics likely accelerated the transition to turbulence, but neither identified them as T&K dynamics nor explored them in detail.

Additional evidence of the potential importance of KHI T&K dynamics was provided by initial idealized LES and DNS of these dynamics demonstrating their dominance of the vorticity dynamics driving turbulence transitions (F21) and significantly elevated energy dissipation rates extending to late times (F22b). These influences are further reinforced by the idealized MS dynamics described here, in which strictly 2D initial GW superpositions appear to frequently (perhaps inevitably) enable 3D KHI T&K dynamics where Ri is sufficiently small and Re is sufficiently large. In the case described here, KHI T&K dynamics yielded energy dissipation rates exceeding those due to coincident GW breaking, despite the idealized Boussinesq flow precluding continuing GW energy fluxes from below.

Another implication of KHI T&K dynamics is potentially enhanced mixing, and enhanced deposition of energy and momentum, as these depend on the environments in which turbulence arises. In the case of GW breaking, turbulence and mixing occurs primarily in the GW phase that is approaching, or already exceeds, overturning, contributing to the inference of a turbulence Prandtl number of ~2 (Fritts and Dunkerton 1985; Coy and Fritts 1988; McIntyre 1989; Garcia et al. 2014; Liu 2021). KHI, on the other hand, and potentially enhanced mixing and transport due to T&K dynamics, may prove to be significantly more efficient, given that KHI arise on the most highly stratified sheets in an S&L environment, but these effects remain to be quantified. Such events appear to provide one explanation for "a stable and well-ordered flow [that] can develop intense and sporadic bursts of turbulent activity that disappear slowly in time" noted by Rorai et al. (2014).

There are very few previous high-resolution DNS of MS GW dynamics performed at sufficiently high Re to enable descriptions of 1) multiple superposed GWs, 2) embedded small-scale GW breaking and/or KHI, and 3) local high-Re KHI dynamics driving resolved turbulence at smaller scales. We are only aware of our own MS GW studies (F13; FW13; F16), and this study performed for $\mathrm{Re}_0 = \lambda_z^2/\nu T_b$ increasing from 50000 to 150000 to date. Of these, the current study employing the largest Re is potentially most representative of S&L flows for larger GW $\lambda_z \sim 1$–3, 3–10, and 10–30 km, and assumed GW intrinsic frequencies $\omega_i \sim 0.03$–$0.3N$, at altitudes of ~30, 60, and 90 km, respectively.

Related studies exhibiting transitions to turbulence in a large-amplitude inertia–GW (IGW) environment employing a hierarchy of 2D and 3D DNS were described by Fruman and Achatz (2012), Remmler et al. (2013), and Fruman et al. (2014). Prior to the 3D transition to turbulence in these studies, the larger-scale IGW was seen to exhibit an initial, local singular vector suggesting an apparent localized KHI feature and similar events in regions of enhanced stratification and shear as the IGW flow evolved greater complexity; see Figs. 4, 5, 10, and 11 of Fruman et al. (2014). These results appear to confirm the potential for local KHI to arise at specific sites within large-scale, and large-amplitude, IGWs that dominate observed atmospheric temperature and wind variances from the troposphere into the MLT.

KHI T&K dynamics revealed in the MS DNS described here also have similarities to those seen arising in a more idealized, higher-resolution, DNS of multi-KH billow T&K dynamics in a periodic domain that excludes GW influences. Initial studies of these more focused KHI T&K dynamics and energetics by F22a and F22b extended their descriptions deep into the turbulence inertial range and quantified their dynamics and implications for enhanced ε. Importantly, these studies did not address T&K dynamics arising where KH billows are misaligned along their axes, as addressed in the idealized LES by F21. However, they are seen to be major contributors to the dynamics arising in larger- and smaller-scale T&K events in the current DNS shown in Figs. 11–13, suggesting additional T&K sources of enhanced ε and mixing in more realistic environments.

6. Conclusions

Extensive observational evidence for KHI T&K dynamics in the atmosphere and oceans reviewed by F23a reveals KHI T&K dynamics on highly stratified sheets to be widespread, and potentially ubiquitous, where they arise with sufficiently large Re. This is especially the case in the atmosphere, where GWs propagating upward from sources at lower altitudes provide sustained energy inputs that induce and intensify S&L features enabling local KHI T&K dynamics at higher altitudes.

Limited modeling studies of KHI T&K dynamics to date for idealized flows and others arising from initial noise seeds have revealed a diversity of responses. But these studies surely have neither identified nor quantified the full range of T&K dynamics and their implications for enhanced turbulence and mixing for the wide range of Ri and Re characterizing atmospheric S&L flows. One example noted above is the T&K dynamics of two billow cores linking to one, as addressed using LES by F21 and seen to occur in the MS DNS discussed above. Some of these additional T&K dynamics are addressed via DNS by F23b for Ri = 0.1 and Re_0 = 500–5000. However, multiple aspects of these dynamics remain to be explored, including the following:

1) influences of background GWs, based on the evidence described by T02 and F23a;
2) their forms, intensities, and evolutions at smaller and larger Ri, and true Pr for the atmosphere and oceans;
3) their implications for elevated ε and mixing for varying environments and parameters;
4) the turbulence fluxes of energy, enstrophy, and helicity that accompany the initial, larger-scale, "twist wave" dynamics that appear to drive the cascade to smaller scales in these T&K dynamics (e.g., F21; F22a); and
5) their potential to arise in magnetohydrodynamics, where KHI are known to play important roles in many applications and environments are complex, but which are outside our expertise.

Acknowledgments. Research described here was performed under AFOSR Grant FA9550-18-1-0009 and NSF Grants AGS-2017263, AGS-2032678, AGS-2128443, and AGS-2129222 cited in GEMS. We thank the DoD HPCMP for access to computational resources that enabled this modeling study. We also thank three reviewers and JAS Editor Peter Bartello for multiple comments that improved the paper and acknowledge Dr. J. Werne and NWRA for our previous use of the Triple code.

Data availability statement. DNS modeling data reside on the DoD High Performance Computing Modernization Program systems, where all analyses and imaging were performed. These data comprise very large data volumes (a single field at the peak resolution at one time is ~100 GB in single precision, binary form), and these DoD systems are not open access. Hence these data are not publicly accessible. For very limited portions of these data, the authors can assist in providing data for specific research interests.

REFERENCES

Balaras, E., U. Piomelli, and J. M. Wallace, 2001: Self-similar states in turbulent mixing layers. *J. Fluid Mech.*, **446**, 1–24, https://doi.org/10.1017/S0022112001005626.

Balsley, B. B., D. A. Lawrence, D. C. Fritts, L. Wang, K. Wan, and J. Werne, 2018: Fine structure, instabilities, and turbulence in the lower atmosphere: High-resolution in situ slant-path measurements with the DataHawk UAV and comparisons with numerical modeling. *J. Atmos. Oceanic Technol.*, **35**, 619–642, https://doi.org/10.1175/JTECH-D-16-0037.1.

Baumgarten, G., and D. C. Fritts, 2014: Quantifying Kelvin-Helmholtz instability dynamics observed in noctilucent clouds: 1. Methods and observations. *J. Geophys. Res. Atmos.*, **119**, 9324–9337, https://doi.org/10.1002/2014JD021832.

Caulfield, C. P., S. Yoshida, and W. R. Peltier, 1996: Secondary instability and three-dimensionalization in a laboratory accelerating shear layer with varying density differences. *Dyn. Atmos. Oceans*, **23**, 125–138, https://doi.org/10.1016/0377-0265(95)00418-1.

Comte, P., J. H. Silvestrini, and P. Begou, 1998: Streamwise vortices in large-eddy simulations of mixing layers. *Eur. J. Mech.*, **17B**, 615–637, https://doi.org/10.1016/S0997-7546(98)80016-2.

Coy, L., and D. C. Fritts, 1988: Gravity wave heat fluxes: A Lagrangian approach. *J. Atmos. Sci.*, **45**, 1770–1780, https://doi.org/10.1175/1520-0469(1988)045<1770:GWLFAL>2.0.CO;2.

Dalaudier, F., C. Sidi, M. Crochet, and J. Vernin, 1994: Direct evidence of "sheets" in the atmospheric temperature field. *J. Atmos. Sci.*, **51**, 237–248, https://doi.org/10.1175/1520-0469(1994)051<0237:DEOITA>2.0.CO;2.

Doddi, A., D. Lawrence, D. Fritts, L. Wang, T. Lund, W. Brown, D. Zajic, and L. Kantha, 2022: Instabilities, Dynamics, and Energetics accompanying Atmospheric Layering (IDEAL): High-resolution in situ observations above the nocturnal boundary layer. *Atmos. Meas. Tech.*, **15**, 4023–4045, https://doi.org/10.5194/amt-15-4023-2022.

Drazin, P. G., 1958: The stability of a shear layer in an unbounded heterogeneous inviscid fluid. *J. Fluid Mech.*, **4**, 214–224, https://doi.org/10.1017/S0022112058000409.

Fritts, D. C., and T. J. Dunkerton, 1985: Fluxes of heat and constituents due to convectively unstable gravity waves. *J. Atmos. Sci.*, **42**, 549–556, https://doi.org/10.1175/1520-0469(1985)042<0549:FOHACD>2.0.CO;2.

——, and L. Wang, 2013: Gravity wave–fine structure interactions. Part II: Energy dissipation evolutions, statistics, and implications. *J. Atmos. Sci.*, **70**, 3735–3755, https://doi.org/10.1175/JAS-D-13-059.1.

——, S. Arendt, and O. Andreassen, 1998: Vorticity dynamics in a breaking internal gravity wave. Part 2. Vortex interactions and transition to turbulence. *J. Fluid Mech.*, **367**, 47–65, https://doi.org/10.1017/S0022112098001633.

——, L. Wang, J. Werne, T. Lund, and K. Wan, 2009: Gravity wave instability dynamic at high Reynolds numbers. Part II: Turbulence evolution, structure, and anisotropy. *J. Atmos. Sci.*, **66**, 1149–1171, https://doi.org/10.1175/2008JAS2727.1.

——, ——, and ——, 2013: Gravity wave–fine structure interactions. Part I: Influences of fine structure form and orientation on flow evolution and instability. *J. Atmos. Sci.*, **70**, 3710–3734, https://doi.org/10.1175/JAS-D-13-055.1.

——, G. Baumgarten, K. Wan, J. Werne, and T. Lund, 2014: Quantifying Kelvin-Helmholtz instability dynamics observed in noctilucent clouds: 2. Modeling and interpretation of observations. *J. Geophys. Res. Atmos.*, **119**, 9324–9337, https://doi.org/10.1002/2014JD021833.

——, L. Wang, M. A. Geller, D. A. Lawrence, J. Werne, and B. B. Balsley, 2016: Numerical modeling of multi-scale dynamics at a high Reynolds number: Instabilities, turbulence, and an assessment of Ozmidov and Thorpe scales. *J. Atmos. Sci.*, **73**, 555–578, https://doi.org/10.1175/JAS-D-14-0343.1.

——, S. A. Wieland, T. S. Lund, S. A. Thorpe, and J. H. Hecht, 2021: Kelvin-Helmholtz billow interactions and instabilities in the mesosphere over the Andes Lidar Observatory: 2. Modeling and interpretation. *J. Geophys. Res. Atmos.*, **125**, e2020JD033412, https://doi.org/10.1029/2020JD033412.

——, L. Wang, T. S. Lund, and S. A. Thorpe, 2022a: Multi-scale dynamics of Kelvin–Helmholtz instabilities. Part 1: Secondary instabilities and the dynamics of tubes and knots. *J. Fluid Mech.*, **941**, A30, https://doi.org/10.1017/jfm.2021.1085.

——, ——, S. A. Thorpe, and T. S. Lund, 2022b: Multi-scale dynamics of Kelvin–Helmholtz instabilities. Part 2: Energy dissipation rates, evolutions, and statistics. *J. Fluid Mech.*, **941**, A31, https://doi.org/10.1017/jfm.2021.1086.

——, and Coauthors, 2023a: Kelvin–Helmholtz instability “tube” and “knot” dynamics. Part I: Expanding observational evidence of occurrence and environmental influences. *J. Atmos. Sci.*, **80**, 2419–2437, https://doi.org/10.1175/JAS-D-22-0189.1.

Fruman, M. D., and U. Achatz, 2012: Secondary instabilities in breaking inertia–gravity waves. *J. Atmos. Sci.*, **69**, 303–322, https://doi.org/10.1175/JAS-D-10-05027.1.

——, S. Remmler, U. Achatz, and S. Hickel, 2014: On the construction of a direct numerical simulation of a breaking inertia-gravity wave in the upper mesosphere. *J. Geophys. Res. Atmos.*, **119**, 11 613–11 640, https://doi.org/10.1002/2014JD022046.

Garcia, R. R., M. López-Puertas, B. Funke, D. R. Marsh, D. E. Kinnison, A. K. Smith, and F. Gonzalez-Galindo, 2014: On the distribution of CO_2 and CO in the mesosphere and lower thermosphere. *J. Geophys. Res. Atmos.*, **119**, 5700–5718, https://doi.org/10.1002/2013JD021208.

Gregg, M. C., E. A. D’Asaro, J. J. Riley, and E. Kunze, 2018: Mixing efficiency in the ocean. *Annu. Rev. Mar. Sci.*, **10**, 443–473, https://doi.org/10.1146/annurev-marine-121916-063643.

Hecht, J. H., and Coauthors, 2014: The life cycle of instability features measured from the Andes Lidar Observatory over Cerro Pachon on 24 March 2012. *J. Geophys. Res. Atmos.*, **119**, 8872–8898, https://doi.org/10.1002/2014JD021726.

——, D. C. Fritts, L. J. Gelinas, R. J. Rudy, R. L. Walterscheid, and A. Z. Liu, 2021: Kelvin-Helmholtz billow interactions and instabilities in the mesosphere over the Andes Lidar Observatory: 1. Observations. *J. Geophys. Res. Atmos.*, **126**, e2020JD033414, https://doi.org/10.1029/2020JD033414.

Jeong, J., and F. Hussain, 1995: On the identification of a vortex. *J. Fluid Mech.*, **285**, 69–94, https://doi.org/10.1017/S0022112095000462.

Kantha, L., D. Lawrence, H. Luce, H. Hashiguchi, T. Tsuda, R. Wilson, T. Mixa, and M. Yabuki, 2017: Shigaraki UAV-Radar Experiment (ShUREX): Overview of the campaign with some preliminary results. *Prog. Earth Planet. Sci.*, **4**, 19, https://doi.org/10.1186/s40645-017-0133-x.

Kjellstrand, C. B., and Coauthors, 2022: Multi-scale Kelvin-Helmholtz instability dynamics observed by PMC-Turbo on 12 July 2018: 1. Secondary instabilities and billow interactions. *J. Geophys. Res. Atmos.*, **127**, e2021JD036232, https://doi.org/10.1029/2021JD036232.

Liu, H.-L., 2021: Effective vertical diffusion by atmospheric gravity waves. *Geophys. Res. Lett.*, **48**, e2020GL091474, https://doi.org/10.1029/2020GL091474.

Luce, H., M. Crochet, F. Dalaudier, and C. Sidi, 1995: Interpretation of VHF ST radar vertical echoes from in situ temperature sheet observations. *Radio Sci.*, **30**, 1003–1025, https://doi.org/10.1029/95RS00713.

——, L. Kantha, M. Yabuki, and H. Hashiguchi, 2018: Atmospheric Kelvin–Helmholtz billows captured by the MU radar, lidars and a fish-eye camera. *Earth Planets Space*, **70**, 162, https://doi.org/10.1186/s40623-018-0935-0.

Mashayek, A., and W. R. Peltier, 2012a: The “zoo” of secondary instabilities precursory to stratified shear transition. Part 1. Shear aligned convection, pairing, and braid instabilities. *J. Fluid Mech.*, **708**, 5–44, https://doi.org/10.1017/jfm.2012.304.

——, and ——, 2012b: The “zoo” of secondary instabilities precursory to stratified shear transition. Part 2. The influence of stratification. *J. Fluid Mech.*, **708**, 45–70, https://doi.org/10.1017/jfm.2012.294.

McIntyre, M. E., 1989: On dynamics and transport near the polar mesopause in summer. *J. Geophys. Res.*, **94**, 14 617–14 628, https://doi.org/10.1029/JD094iD12p14617.

Moin, P., and K. Mahesh, 1998: Direct numerical simulation: A tool in turbulence research. *Annu. Rev. Fluid Mech.*, **30**, 539–578, https://doi.org/10.1146/annurev.fluid.30.1.539.

Muschinski, A., and C. Wode, 1998: First in situ evidence for coexisting submeter temperature and humidity sheets in the lower free troposphere. *J. Atmos. Sci.*, **55**, 2893–2906, https://doi.org/10.1175/1520-0469(1998)055<2893:FISEFC>2.0.CO;2.

Pope, S. B., 2000: *Turbulent Flows.* Cambridge University Press, 802 pp., https://doi.org/10.1017/CBO9780511840531.

Remmler, S., M. D. Fruman, and S. Hickel, 2013: Direct numerical simulation of a breaking inertia–gravity wave. *J. Fluid Mech.*, **722**, 424–436, https://doi.org/10.1017/jfm.2013.108.

Rorai, C., P. D. Mininni, and A. Pouquet, 2014: Turbulence comes in bursts in stably stratified fluids. *Phys. Rev. E*, **89**, 043002, https://doi.org/10.1103/PhysRevE.89.043002.

Scorer, R., 1951: Billow clouds. *Quart. J. Roy. Meteor. Soc.*, **77**, 235–240, https://doi.org/10.1002/qj.49707733208.

Spalart, P. R., R. D. Moser, and M. M. Rogers, 1991: Spectral methods for the Navier-Stokes equations with one infinite and two periodic directions. *J. Comput. Phys.*, **96**, 297–324, https://doi.org/10.1016/0021-9991(91)90238-G.

Szewczyk, A., B. Strelnikov, M. Rapp, I. Strelnikova, G. Baumgarten, N. Kaifler, T. Dunker, and U.-P. Hoppe, 2013: Simultaneous observations of a mesospheric inversion layer and turbulence during the ECOMA-2010 rocket campaign. *Ann. Geophys.*, **31**, 775–785, https://doi.org/10.5194/angeo-31-775-2013.

Thorpe, S. A., 1973a: Experiments on instability and turbulence in a stratified shear flow. *J. Fluid Mech.*, **61**, 731–751, https://doi.org/10.1017/S0022112073000911.

——, 1973b: Turbulence in stably stratified fluids: A review of laboratory experiments. *Bound.-Layer Meteor.*, **5**, 95–119, https://doi.org/10.1007/BF02188314.

——, 1985: Laboratory observations of secondary structures in Kelvin-Helmholtz billows and consequences for ocean mixing. *Geophys. Astrophys. Fluid Dyn.*, **34**, 175–199, https://doi.org/10.1080/03091928508245442.

——, 1987: Transitional phenomena and the development of turbulence in stratified fluids: A review. *J. Geophys. Res.*, **92**, 5231–5248, https://doi.org/10.1029/JC092iC05p05231.

——, 2002: The axial coherence of Kelvin–Helmholtz billows. *Quart. J. Roy. Meteor. Soc.*, **128**, 1529–1542, https://doi.org/10.1002/qj.200212858307.

Wang, L., D. C. Fritts, B. P. Williams, R. A. Goldberg, F. J. Schmidlin, and U. Blum, 2006: Gravity waves in the middle atmosphere during the MaCWAVE winter campaign: Evidence of mountain wave critical level encounters. *Ann. Geophys.*, **24**, 1209–1226, https://doi.org/10.5194/angeo-24-1209-2006.

Watanabe, T., and K. Nagata, 2021: Large-scale characteristics of a stably stratified turbulent shear layer. *J. Fluid Mech.*, **927**, A27, https://doi.org/10.1017/jfm.2021.773.

Witt, G., 1962: Height, structure and displacements of noctilucent clouds. *Tellus*, **14**, 1–18, https://doi.org/10.3402/tellusa.v14i1.9524.

Woods, J. D., 1968: Wave-induced shear instability in the summer thermocline. *J. Fluid Mech.*, **32**, 791–800, https://doi.org/10.1017/S0022112068001035.